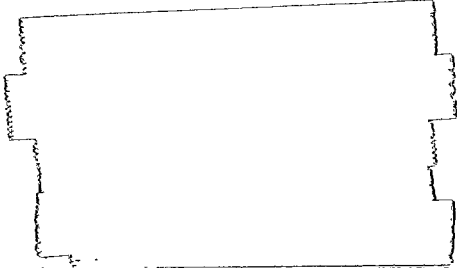


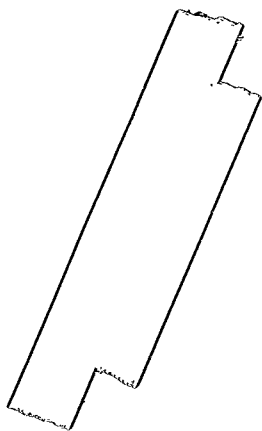
FACILITY FORM 802

N65-32722	
(ACCESSION NUMBER)	(THRU)
109	1
(PAGES)	(CODE)
CD, 64459	31
(NASA CR OR TMX OR AD NUMBER)	(CATEGORY)



CENTER FOR SPACE RESEARCH
MASSACHUSETTS INSTITUTE OF TECHNOLOGY





STUDY OF A SMALL SOLAR PROBE
(Sunblazer)
Part II

SPACECRAFT AND PAYLOAD DESIGN

PR-5255-5

July 1, 1965

7-1-64 fo 6-30-65

PRICES SUBJECT TO CHANGE

MASSACHUSETTS INSTITUTE OF TECHNOLOGY
CENTER FOR SPACE RESEARCH

STUDY OF A SMALL SOLAR PROBE
(Sunblazer)

Part II. Spacecraft and Payload Design

by

R. H. Baker

S. Cohen

W. W. Cooper

D. H. Galvin

J. V. Harrington

W. T. Higgins

R. S. Taylor

July 1, 1965

Work done under
NATIONAL AERONAUTICS AND SPACE ADMINISTRATION
GRANT NASr-249

SUMMARY REPORT ON THE
STUDY OF A SMALL SOLAR PROBE

Part II. Spacecraft and Payload Design

I. Spacecraft

A. General Design Considerations

The Sunblazer spacecraft is a light-weight structure (about 10 pounds) designed to transmit high peak power (about 1 kw) RF bursts at 100 MC and 300 MC and capable of operating for a minimum of two years in the spacecraft environment existing in the region between one A.U. and one-half A.U. The thermal balance problem at 0.5 A.U. and the need to generate and radiate power at the lowest possible weight suggested a radially oriented spacecraft, while the relatively long duration of the experiment argued for a simple electronic design that would provide substantially increased longevity.

The spacecraft configuration as depicted in Fig. 1 is a radially oriented platform consisting of a circular front plate as a platform for solar cell arrays, joined to a cylindrical shell which serves both as a thermal radiator and as a housing for the electronics. Located on an extended boom is the solar vane composed of a cylindrical shell, which is hollow to present a minimum-capture cross-section to thermal energy radiated from the spacecraft. The solar pressure acting on the vane provides the radial restoring torque. This spacecraft geometry, whose details are described in the next section, was selected over other possible configurations such as unstabilized polyhedrons and a stabilized

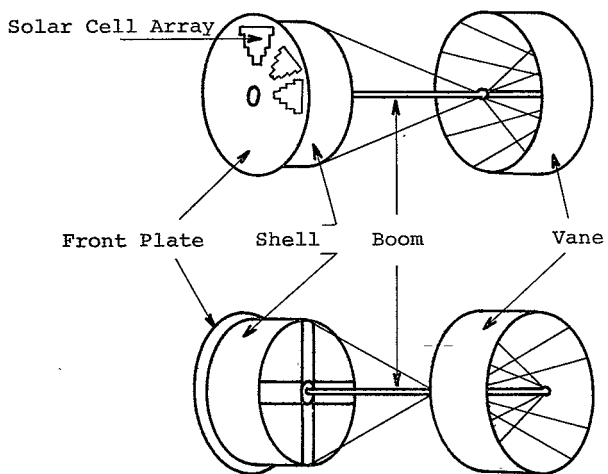


Figure 1

SPACECRAFT CONFIGURATION

"two flat-plate sandwich" structure. The present configuration was dictated by the relatively large solar cell weight penalty of the unoriented compared to the oriented configuration and because of the geometry selected has good heat transfer properties as well as a favorable mass distribution for a solar-pressure oriented system. In addition, the central hub-spoke-shell arrangement offers several important advantages in relation to electronic packaging for minimum weight.

B. Spacecraft Structure

1. Mechanical structure

a. General considerations. The maximum dimensions determined by the airframe geometry of the scout-like launch vehicle for the Sunblazer spacecraft provides a cylindrical shape confined to a 24-in. diameter by 24-in. in height, which represents 10,828 in.³ of volume.

The maximum payload weight as a function of a required terminal velocity of 40,000 ft/sec was calculated to be about 15 pounds.

Initial investigations indicated that a spherical, nonoriented vehicle of 20 in. in diameter could provide an effective solar cell area which would be capable of delivering about 13 watts of power, but would consume 80 pct or more of total payload weight in structure and solar cells. This weight burden, combined with other experimental considerations, determined the need for a solar radii-oriented device.

Since a minimum of 10 watts of converted power was established as the basic requirement, a solar cell area of 178.6 in.² is required for an oriented vehicle. In addition, a thermal relief area in close proximity to the solar cells which amounts to about 40 pct of the cell area can be achieved and readily accommodated within the confines of the 24-in. diameter cylinder.

A 20-in. diameter mounting plate for the solar cells which includes 40 pct obverse and 100 pct reverse emissive areas does not provide sufficient radiation to compensate for the thermal input. To overcome this deficiency, an additional rear circular radiator fin, 5 in. in height and 15 in. in diameter, provides an external surface-radiating area which increases the total by 57 pct to establish a total ratio of thermally emissive area to solar cell area of about 3.7 to 1.

The generalized shape of the Sunblazer payload is, therefore, determined by the constraints of the launch vehicle, the power requirements, and the surfaces required for passive thermal control.

b. Spacecraft structure. In order to obtain interchangeability of a portion of the total solar cell array, and to isolate them electrically in natural building blocks, the basic platform is divided into 45° segments.

Available silicon solar cells (1 x 2 cm) will produce at 1 A.U. a current of 53 milliamperes at 420 millivolts at 30° C. In order to obtain a DC input of about 30 volts to the DC-to-DC converter an array of 72 series-connected cells is placed

on each of the eight segments. These arrays connected in parallel produce about 12.4 watts at 1 A.U. as an input power to the converter.

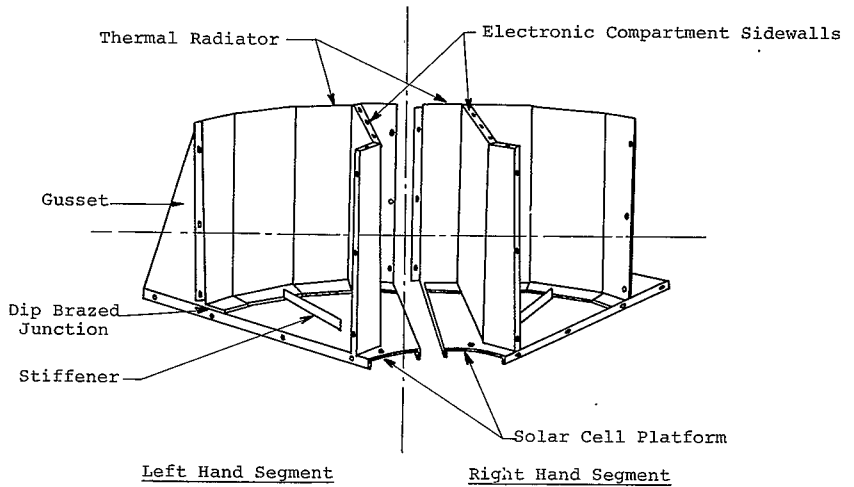
As shown in Fig. 2, four right- and left-hand segments are used to form the platform and radiator structure.

The 45° segments are of flanged sheet metal construction consisting of 5 basic parts: the solar cell platform, the thermal radiator, the electronic compartment sidewall, a platform stiffener, and platform-radiator gusset. Various gauges of 6061-T6 aluminum were used for the parts, with the chosen thickness reflecting the various needs for a mechanical integrity and thermal conductance.

A general observation from a review of the structural analysis, that utilized column-buckling formulas with a substitution in the formulas of an "equivalent slenderness ratio" with loadings of 150 g's, indicate that the materials are stressed very low, and demonstrate relatively large safety factors. The minimum safety factor is 1.3 in the noncritical compartment sidewall.

The individual parts of the segment are unitized by a dip-brazing process principally to insure a low-resistance thermal junction between the solar-cell platform and its associated radiating fin. The eight segments are assembled in the horizontal and the vertical flanged interfaces with 4-40 stainless steel screws and elliptical lock nuts.

The compartment sidewalls outline a cruciform container for the electronics. This configuration was chosen since



BASIC SUNBLAZER SPACECRAFT
FABRICATION

Figure 2

it provides a good match to the platform thermal radiation, exposes the minimum profile of the electronics to thermal radiation, and allows independent thermal control of the electronics as well as providing a means for eliminating connectors in the subsystem interconnections.

The electronics subsystems are positioned at 90° intervals around a central, hollow, laminated hub which performs dually as a mechanical support structure and as an electrical conduct system.

Each of the subsystem modules are constructed around a basic interconnecting card which performs electrically as a conductor terminal and shield, and which functions mechanically as a secondary support structure for the individual module as well as being the main thermal conductor to the electronic chassis radiator.

In the RF modules, boards containing the components are mounted perpendicular to, and intersecting with, the interconnection card in an "egg crate" manner, to provide three-dimensional mounting versatility for the RF components and additional shielding and ground planes within the module.

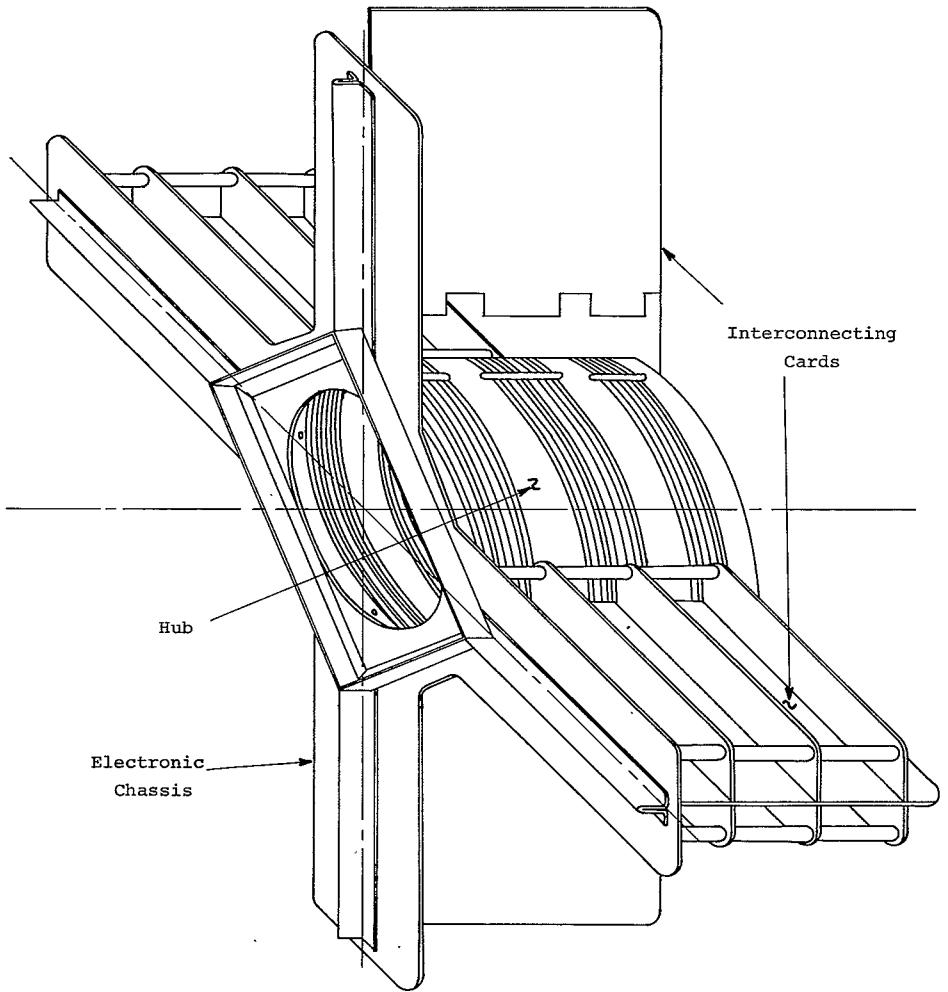
The digital coding subsystem is mounted directly on the interconnecting card, utilizing individual circuit modules connected by printed wiring. This area remains flexible for packaging discrete components and hybrid integrated PPC¹ circuitry.

As shown in Fig. 3, all subsystem modules are mechanically unitized by a cruciform electronic chassis, which

1. See "Pulsed Powered Circuits," TR-65-1, M.I.T. Center for Space Research.

ELECTRONIC PACKAGE

Figure 3



acts as the main support, and thermal heat sink and radiator for the system.

This system assembly is thermally isolated from the solar cell platform and radiator by insulating gaskets at the fastening junction, and by a low emissive surface coating on the inner compartment walls.

Subsystem interwiring shown in Fig. 4 indicates that less than 20 internal system wires and less than 30 external sensor wires are required for the total electronic system.

The beacon transponder has self-contained battery power, digital coding system, and an independent sensor system. In the interest of reliability, the two systems have independent, nonswitched telemetry transducers.

c. Weight. A breakdown of the electrical system weight shows about 60 pct of the total allotted to power and storage, 30 pct to the main RF pulser, and 10 pct to the beacon transponder. See Table I.

d. Sail structure. The solar sail structure design must minimize weight, maximize the projected area to the sun, and have a large displacement from the main electronic payload while maintaining mechanical integrity during the launch phase.

A cylindrical sail of the same diameter as the solar cell platform achieves the desired design. The fabrication of the basic sail is composed of two hoop stiffeners made from 1/4-in. aluminum tubing to which a rim of 0.015 in. thick by 8 in. wide aluminum sheeting is bonded with aluminized epoxy. This assembly

Figure 4 BASIC INTERCONNECTIONS

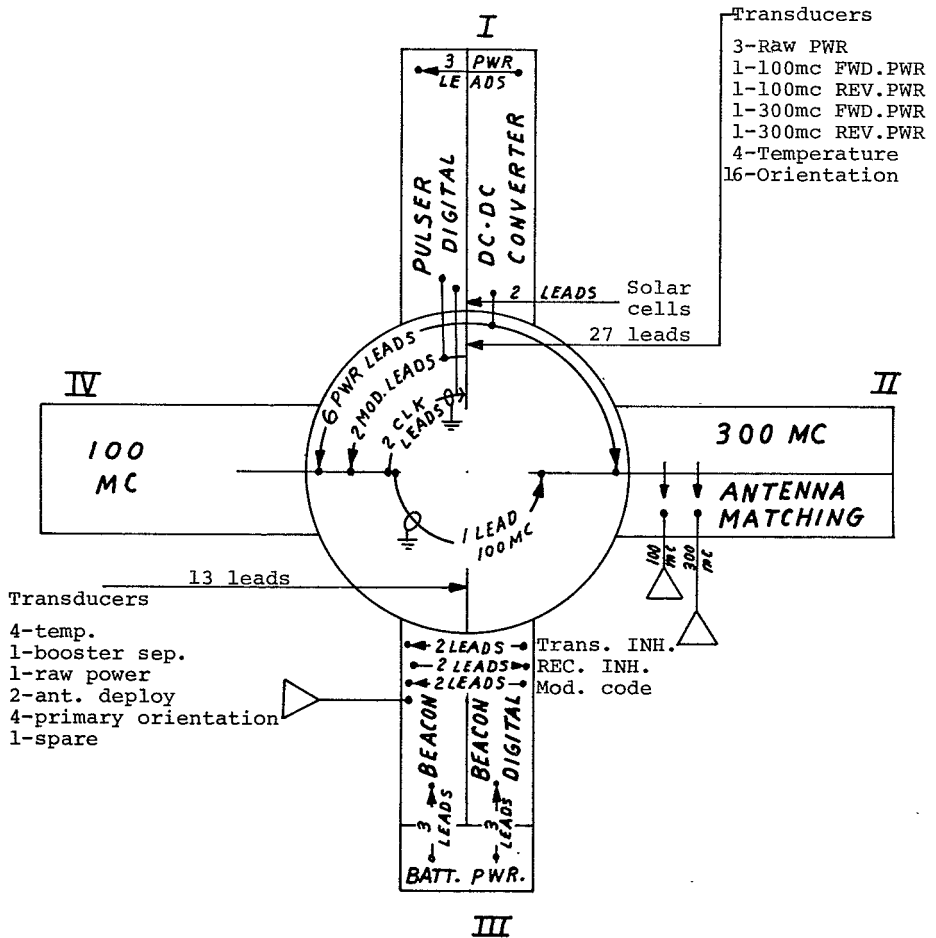


TABLE I. Electrical System Weight Distribution

Power and Storage

Capacitor =	949.1 gm
Solar cells =	384.8 gm
DC-to-DC converter =	360.0 gm
Total	1693.9 gm

Main RF Pulser

RF power =	430.4 gm
RF source =	222.8 gm
Digital coding =	114.8 gm
Antennae =	40.0 gm
Total	808.0 gm

Transponder

Receiver-Transmitter circuitry =	130.7 gm
Digital coding =	80.0 gm
Batteries =	50.0 gm
Total	260.7 gm

Total Electrical Weight

Power and storage =	1693.9 gm
Main RF pulser =	808.0 gm
Transponder =	260.7 gm
System total	2762.6 gm

This total electrical system weight represents about 44 percent of the total launch weight (spacecraft plus final stage interface equipment and separation mechanism) and about 51 percent of the spacecraft weight.

is referenced to a central mast of 3/8-in. diameter aluminum tubing, which projects from the payload hub, by 16 adjustable tension 0.062-in. diameter stainless steel spokes.

Fig. 5 shows the placement of the spokes to achieve mechanical stability in three axes during the launch phase. The spoke pattern of the upper and lower hoops are displaced by 22.5° to provide a closed, saw-toothed stress pattern on the sail.

The mast and its attached sail are positioned and stabilized by four additional adjustable tension-guying spokes. Fig. 6 shows the projected sail area as a function of sun angle. The graph indicates relatively small loss of projected area due to the shadowing caused by the radiator, despite the proximity of the two surfaces. It is significant that the shadowing decreases most rapidly around the 45° displacement angle, and the maximum sail projection occurs at the relatively large angle of $68^\circ 12'$.

e. Interface and separation mechanism. The present design anticipates the launching of the Sunblazer spacecraft with the solar cell platform facing the final stage motor. This launch attitude has the primary design requirement of providing protection to the solar cells from being impacted by hardware debris that may be generated by escaping parts during separation. The secondary consideration is to maintain a minimum of low-profile interface parts on the solar cell platform which could shadow the solar cell array.

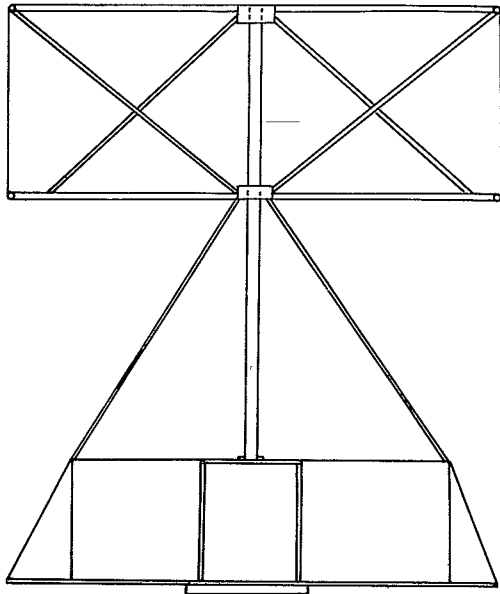
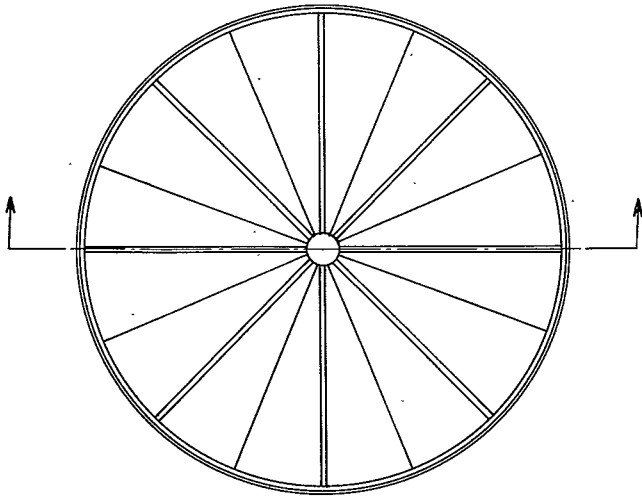


Figure 5 SOLAR SAIL STRUCTURE

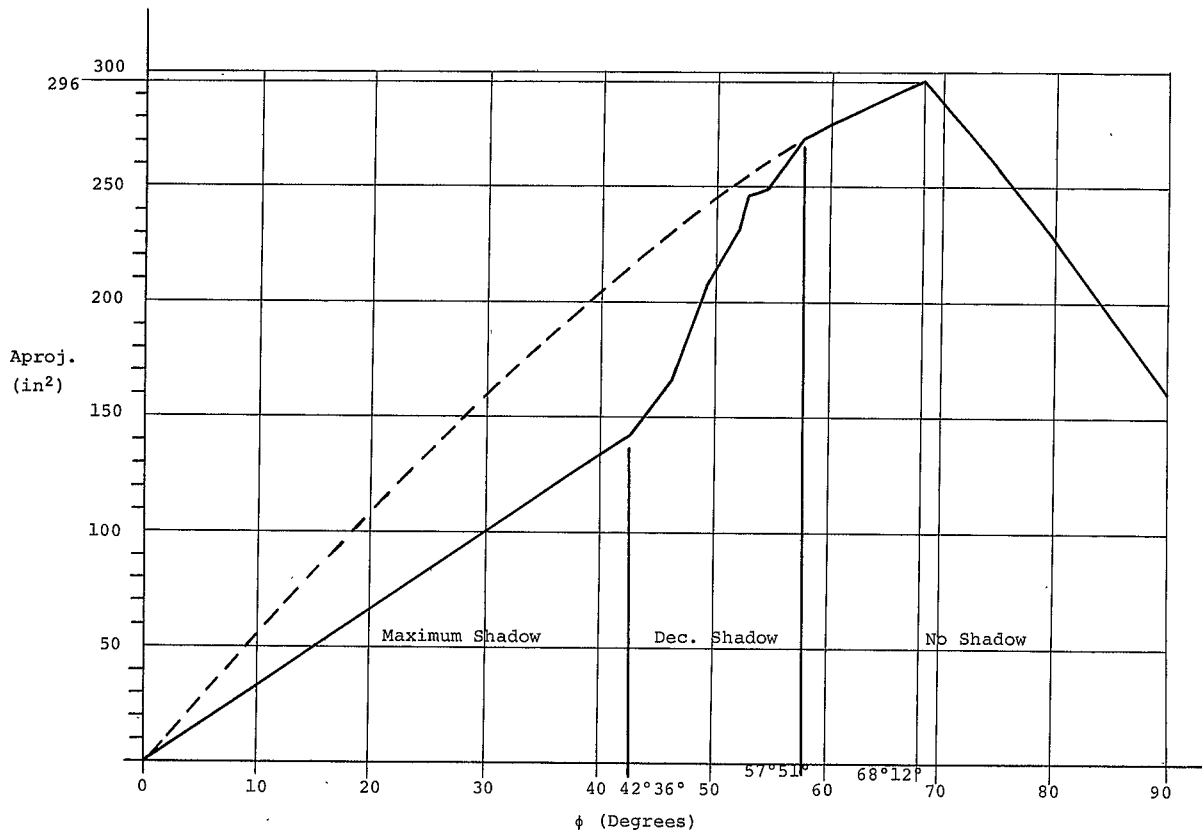


Figure 6. SUN ANGLE vs. PROJECTED SAIL AREA

The purposes of the interface-separation equipment are:

1. To hard-mount and maintain alignment of the vehicle and booster motor in three axes during launch and spin-up;
2. To activate a trigger-release mechanism after burn-out of the booster motor;
3. To provide a linear separation of the vehicle and the motor in the spin axis;
4. To release sufficient energy to obtain about five feet per second separation velocity.

An octamorous assembly designed to mate with the standard forward adapter of the final stage motor provides the required means.

Alignment of the vehicle and motor is achieved by utilizing the existing concave groove and the internal stepped flange of the motor. The cross-sectional view in Fig. 7 shows the details of the interface-separation mechanism.

The final stage forward adapter is affixed to the separation spacer by means of a shaped clamp that mates with the concave outer grooves in the two parts. The clamp is developed from two semi-circular pieces which are bolted together after final assembly.

The machined aluminum separation spacer has eight spring locating and supporting arms, which are machined NEMA-LE, and bolted in place.

The chrome-silicon, square-wire, temperature-stable springs are mechanically fixed to the arms, and housed in a spring

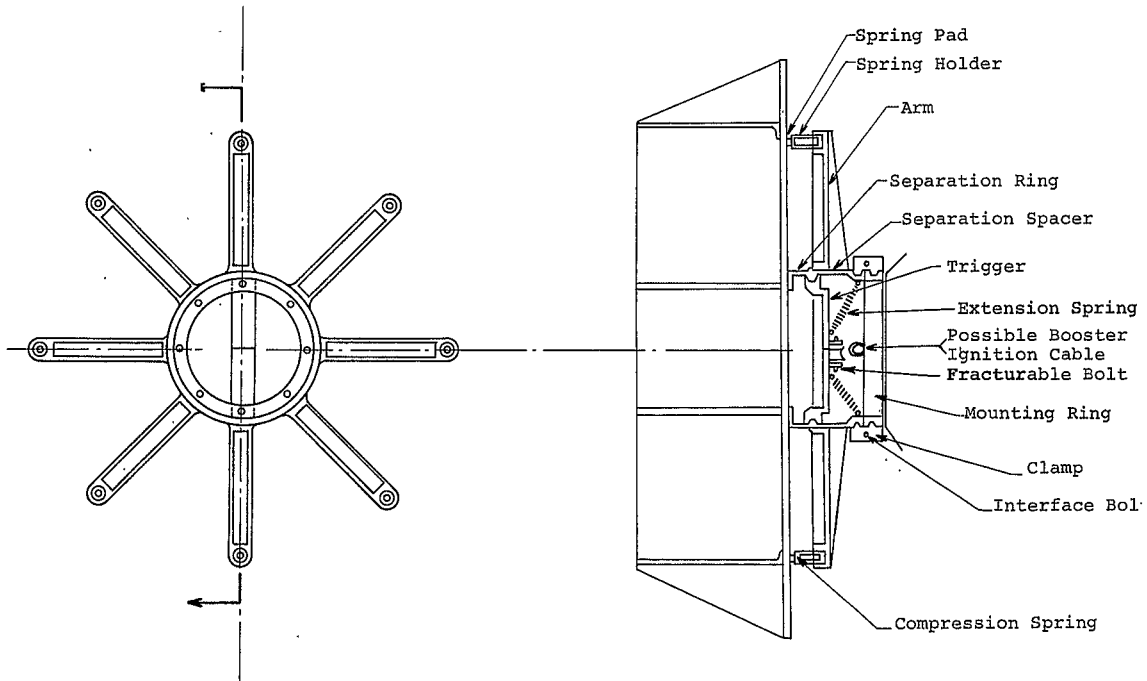


Figure 7

holder (tube). The opposite end of the spring is positioned by a slip fit with a spring pad, the base of which straddles the solar cell platform flanges and is positioned with a through-bolt and lock nut. Projection of the spring pads engages the inner diameters of the spring holders when maximum spring compression occurs. This action radially positions the vehicle and locks its center line in the spin axis of the launch vehicle.

Finally, the upper surface of the separation spacer engages a separation ring which is an integral part of the vehicular assembly. Both of these pieces have internal projections which form a bipartite flange of trapezoidal cross section. It is with these surfaces that the main clamping trigger assembly engages.

The trigger has the following features:

1. The fulcrum is offset by 1/4 in. in height, or 4° of angle;
2. The separation point has a fixed position determined by a $+ 1^\circ$ offset from the perpendicular on each of the trigger pressure surfaces;
3. The trigger is compression loaded into position;
4. Tension springs apply a positive force to the trigger assembly and act as retainers after separation.

The spring compression and trigger placement is accomplished with a loading jig which uses jackscrews to bring the vehicle and separation mechanism into contact. The trigger assembly is positioned manually and locked in place by a single,

nondetonating, fracturable bolt, at which point the loading jig may be removed, and the complete vehicular-separation assembly can be positioned on the booster motor using the two semicircular clamps and associated bolts.

The fracturable bolt is ignited by a delay fuse which in turn is ignited by the booster motor ignition signal with sufficient time delay to encompass the motor burn time by several seconds.

Adequate clearances between the spring support arms and other interference points on the separation ring have been provided to accommodate the passage of the final stage motor-ignition cable and the redundant wiring of the delay fuse.

When the bolt has fractured, the triggers will move in the direction of the motor due to the torque applied by the eight separation springs and the force of the retaining tension springs on the obtuse angle (178°) formed by the vertex of the two triggers. Complete separation of the vehicle will occur within a 25° displacement of the moving parts.

Linearity of separation is assured by the use of multiple springs, and determined by the lateral restraints imposed in them externally by the spring holder and internally by the spring pad in relation to the actinomorphous geometry of the whole.

Design calculations and basic tests of the apparatus indicate a separation velocity of at least 5 ft/sec is realizable without imposing excessive stresses due to spring loading on the vehicle assembly.

The separation ring, which is the largest of the parts that are affixed to the vehicle, will begin to shadow one segment of the solar cells when the intersection of the sun line and the solar platform plane exceeds 45°. When this angle decreases to 17°, approximately 10 pct of the cells on the particular segment will be in shadow.

f. Mechanical weight. The mechanical weight distribution shows about 45 pct of the total used by the platform and radiator, 24 pct by the interface-separation mechanism, 19 pct by the sail assembly, and 12 pct by miscellaneous hardware. See Table II.

g. Special features. Since there exists the possibility of a number of experiments, particular care has been involved in the Sunblazer design to insure versatility and adaptability for modifications and additions of circuitry as needed in future investigations.

The central 3.6-in. diameter hole and the hollow hub behind it contain a volume of 50 in³, which can be used, for example, to mount a pointed experiment sensor.

If the central volume is not sufficient for packaging the pointed experiments' electronics, or additional programming and telemetry are required, the total electronics volume can be increased up to 100 pct without requiring a change in the existing electronic modules.

The "circular" radiator is actually made from a series of flats, whose vertices are located at 15° increments.

TABLE II. Mechanical Weight Distribution

Platform and Radiator Segment (Average)

Radiator =	96	gm
Platform =	56	gm
Compartment wall =	33	gm
Gusset =	12	gm
Stiffener =	2	gm
Brazing =	2.5	gm
	<hr/>	
Total	201.5	gm

Total Platform and Radiator Assembly

$$201.5 \text{ gm} \times 8 = 1612 \text{ gm}$$

Interface-Separation Mechanism

8 Arms =	274	gm
Separation spacer =	218	gm
Clamp =	139	gm
Separation ring =	128	gm
Trigger =	57	gm
Springs & hardware =	48	gm
	<hr/>	
Total	864	gm

Sail

Sheet metal & tubing =	407.6	gm
20 Spokes =	129.3	gm
Mounting plate =	70.4	gm
Mast =	31.3	gm
3 Hubs =	15.0	gm
	<hr/>	
Total	653.6	gm

TABLE II continued

Electro-Mechanical Assembly

Hub =	165.1 gm
Electronic chassis =	122.4 gm
Nuts & bolts =	147.1 gm
	<hr/>
Total	434.6 gm

Total Mechanical Weight

Platform & radiator =	1612.0 gm
Interface-separation mech. =	864.0 gm
Sail =	653.6 gm
Electro-mechanical assembly =	434.6 gm
	<hr/>
Total	3564.2 gm

Complete System Weight

Electrical =	2762.6 gm
Mechanical =	3564.2 gm
	<hr/>
Total	6326.8 gm \approx 14.1lbs

This geometry allows the addition of two or four more compartments to accommodate additional circuitry by merely relocating the compartment sidewalls in the revised assembly. Interconnections to the additional subsystem modules can be accommodated by the hub by relocating or adding additional receptacles for the subsystem interconnecting cards.

2. Thermal characteristics. The essential advantage of an oriented structure stems from the freedom of choice with regard to selection of coating absorbtivity and emissivity for the shaded and unshaded portions of the spacecraft. That is, the coating absorbtivity of the sunlit portion of the spacecraft may be minimized with little regard for the emissivity, consequently minimizing the absorbed energy, while the always shaded coating may be selected only for high emissivity, thereby obtaining maximum reradiation of the already minimized absorbed thermal energy. In addition, the thermal transfer paths may be optimized since the thermal source-sink geometry is fixed for an oriented vehicle which leads to better thermal control per unit mass, which is important for low-mass structure design.

The thermal design of the spacecraft includes the following considerations: first, in order to maximize the generated DC power, the solar cell array is designed to operate at a low temperature by utilizing a low-absorbing gold coating (≈ 0.23) over that area of the front plate not covered by solar cells. Next, the area, thickness, and length of the cylindrical radiator was

designed to maximize the thermal energy transfer (see Appendix A) from the front plate through the cylinder into space.

The spacecraft configuration, illustrated in Fig. 8, was studied to determine the approximate thermal characteristics and establish some initial design parameters.

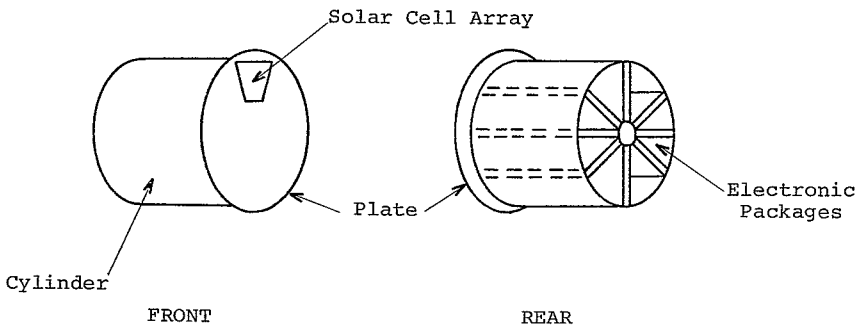


FIG. 8. Spacecraft Configuration

The configuration consists of a plate on which eight groups of seventy-two 1 cm x 2 cm solar cells are equally distributed, a radiating cylinder, and four compartments for electronic packages.

The calculations were made for 0.5 A.U. and 1 A.U. with the following assumptions:

α gold	= 0.23
α solar cells	= 0.78
ϵ solar cells	= 0.835
ϵ radiating surfaces	= 0.85

Various radial locations of the solar array were considered in combination with cylinder diameter. The plate thickness, the cylinder thicknesses, and the electronic package wall thickness considered were 1/32 in., 1/16 in., and 1/64 in. respectively.

The electronic circuits were assumed to be thermally isolated from the package side walls and thermally connected to the rear surface of the package which is exposed to space. This offers the possibility of maintaining a different temperature extending over a narrower range than the basic structure temperature.

Since the results obtained are dependent upon the internal geometry factors, the surface emissivities, and the long-term effects of the space environment on emissivities, a thermal model should be constructed and tested to verify the results as well as investigate various thermal coatings.

Details of the thermal configurations and assumed constants, together with appropriate nomenclature, are given in Fig. 9.

The thermal input at a solar distance of 1 A.U. is given by:

$$H_{IN} = q [(A_{fp} - A_{sc}) \alpha_g + A_{sc} \alpha_{sc}] - P_{DC} \quad [1]$$

where

$$q = 140 \text{ mw/cm}^2 \text{ (solar constant)}$$

$$P_{DC} = 12 \text{ watts}$$

Substituting the appropriate constants of Fig. 9 into Eq. [1] gives:

$$\begin{aligned} H_{IN} &= 140 \times 10^{-3} [(2026-1152)(0.23) + (1152)(0.78)] - 12 \\ &= 142 \text{ watts} \end{aligned} \quad [2]$$

The radiated thermal energy may be expressed as:

$$H_{OUT} = H_{OUT} \text{ (plate)} + H_{OUT} \text{ (cylinder)} \quad [3]$$

Utilizing the nomenclature of Fig. 9, Eq. [3] may be expressed as:

$$\begin{aligned} H_{OUT} \text{ (plate)} &= \sigma [\epsilon_g (A_{fp} - A_{sc}) + \epsilon_{sc} A_{sc} + \epsilon_{ebp} A_{ebp} + \\ &\quad \epsilon_{ibp} A_{ibp}] (T_{P_{ISO}})^4 \end{aligned} \quad [4a]$$

$$\begin{aligned} H_{OUT} \text{ (cylinder)} &= \sigma [\epsilon_{re} A_{re} + \epsilon_{ri} A_{ri} + \epsilon_{sw} A_{sw} + \\ &\quad \epsilon_{es} A_{es}] (T_{R_{ISO}})^4 \end{aligned} \quad [4b]$$

where $\sigma = 5.76 \times 10^{-12} \text{ watts/cm}^2 \text{ } ^\circ\text{K}^4$

$T_{P_{ISO}}$ = equivalent temperature of an isothermal plate

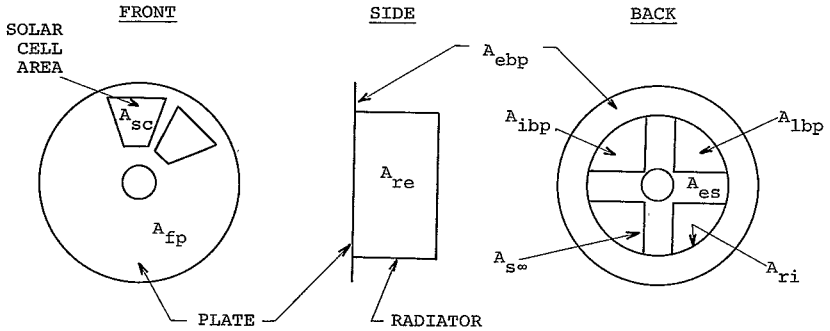
$T_{R_{ISO}}$ = equivalent temperature of an isothermal cylinder radiator

Substituting the appropriate constants in Eq. [4a] and [4b]

gives:

$$H_{OUT} \text{ (plate)} = 0.95 \times 10^{-8} (T_{P_{ISO}})^4 \quad [5a]$$

$$H_{OUT} \text{ (cylinder)} = 1.43 \times 10^{-8} (T_{R_{ISO}})^4 \quad [5b]$$



A_{fp}	= Area of front plate = 2026 cm ²	$\left\{ \begin{array}{l} \alpha_g = 0.23 \\ \epsilon_g = 0.07 \end{array} \right.$
A_{ebp}	= Area of external back plate = 886 cm ²	$\left\{ \begin{array}{l} \alpha_{ebp} = 0 \\ \epsilon_{ebp} = 0.85 \times (0.5) \\ \text{(50% effective)} \end{array} \right.$
A_{ibp}	= Area of internal back plate = 817 cm ²	$\left\{ \begin{array}{l} \alpha_{ibp} = 0 \\ \epsilon_{ibp} = 0.85 \times (0.2) \\ \text{(20% effective)} \end{array} \right.$
A_{sc}	= Area of solar cells = 1152 cm ²	$\left\{ \begin{array}{l} \alpha_{sc} = 0.78 \\ \epsilon_{sc} = 0.835 \end{array} \right.$
A_{re}	= Area radiator external = 1555 cm ²	$\left\{ \begin{array}{l} \alpha_{re} = 0 \\ \epsilon_{re} = 0.85 \end{array} \right.$
A_{ri}	= Area radiator internal = 1297 cm ²	$\left\{ \begin{array}{l} \alpha_{ri} = 0 \\ \epsilon_{ri} = 0.85 \times (0.3) \\ \text{(30% effective)} \end{array} \right.$
A_{sw}	= Area side walls = 1368 cm ²	$\left\{ \begin{array}{l} \alpha_{sw} = 0 \\ \epsilon_{sw} = 0.85 \times (0.3) \\ \text{30% effective)} \end{array} \right.$
A_{es}	= Area of electronic back surface = 817 cm ²	$\left\{ \begin{array}{l} \alpha_{es} = 0 \\ \epsilon_{es} = 0.85 \end{array} \right.$

FIGURE 9

At thermal equilibrium the results of Eq. [5] are numerically equal to those of Eq. [2] or:

$$0.95 \times 10^{-8} (T_{P_{ISO}})^4 + 1.43 \times 10^{-8} (T_{R_{ISO}})^4 = 142 \text{ watts*} \quad [6]$$

The equivalent isothermal front plate and cylindrical radiator temperatures $T_{P_{ISO}}$ and $T_{R_{ISO}}$ may be determined with the aid of Fig. 10.

Fig. 10 shows the temperature gradients of the spacecraft design for "near optimum thermal transfer" (see Appendix A) as a function of temperature (thermal input). By utilizing the results of Eq. [6] and Fig. 10, we get:

$$\left. \begin{aligned} T_{P_{ISO}} &= 287^\circ \text{ K} \\ T_{R_{ISO}} &= 278^\circ \text{ K} \end{aligned} \right\} \text{ at 1 A.U.} \quad [7]$$

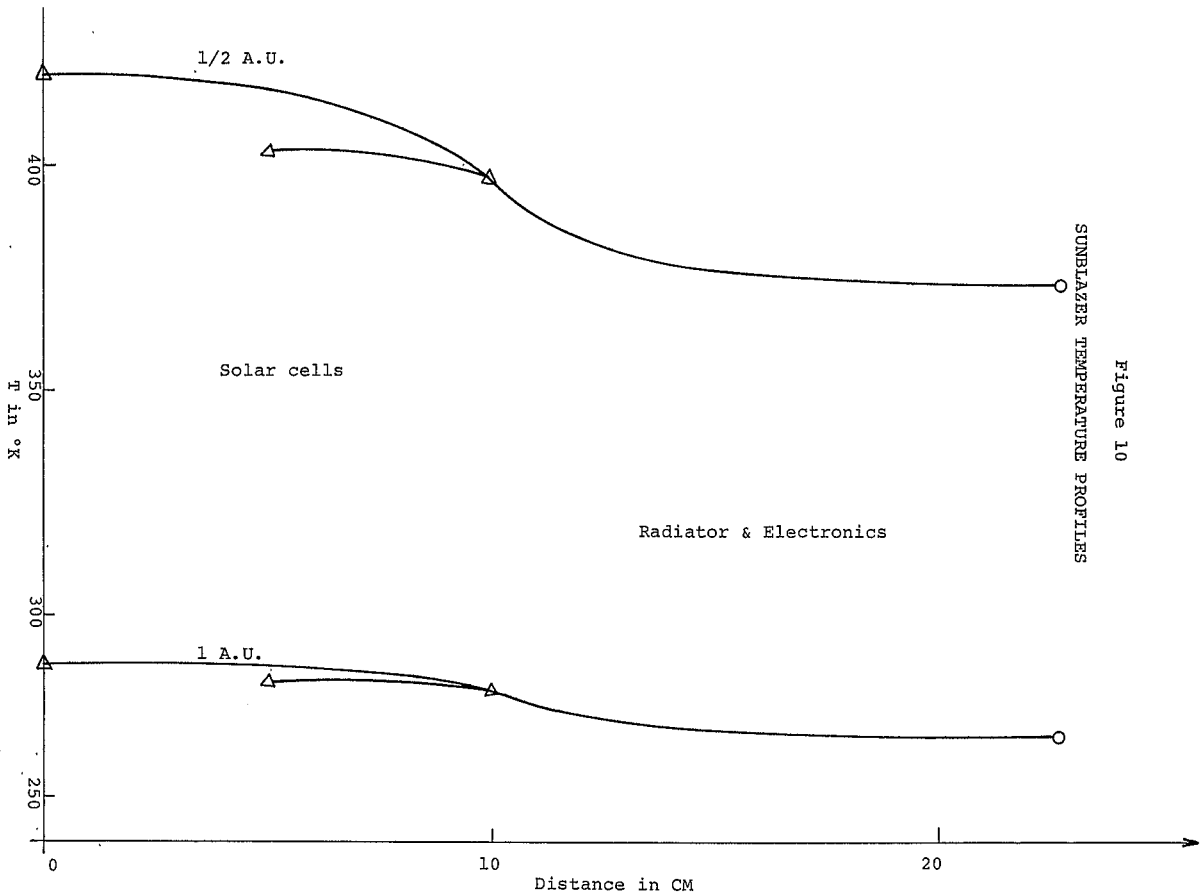
And at 0.5 A.U., where the solar constant is equal to 560×10^{-3} watts/cm², then:

$$0.95 \times 10^{-3} (T_{P_{ISO}})^4 + 1.43 \times 10^{-8} (T_{R_{ISO}})^4 = 590 \text{ watts} \quad [8]$$

and the equilibrium isothermal temperatures are:

$$\left. \begin{aligned} T_{P_{ISO}} &= 410^\circ \text{ K} \\ T_{R_{ISO}} &= 383^\circ \text{ K} \end{aligned} \right\} \text{ at 0.5 A.U.} \quad [9]$$

* The results of Eq. [6] neglect the electronics dissipation within the package. However, this error is negligible.



SUNBLAZER TEMPERATURE PROFILES

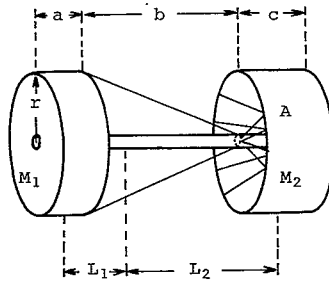
Figure 10

The above results neglect the quantity of thermal energy conducted away and radiated by the stabilization boom and vane assembly, and the effect of the additional radiating surface afforded by the eight stiffeners located along the cylindrical radiator. Also the assigned value of 0.85 for the emissivity of the dark (shaded) surfaces are probably conservative, and therefore the temperature profiles shown in Fig. 10 are considered to be maximum temperatures. If upon experimental evidence this proves to be the case, relatively uncomplicated changes can be made to increase the radiator surface area by adding additional stiffeners, increasing the length of the cylindrical radiator slightly, etc.

3. Spacecraft dynamics

a. Orientation. Two principal orientation schemes were considered for radially orienting the spacecraft, gravity gradient, and solar radiation pressure. While it appears that either method is feasible, solar pressure orientation was selected because, for the contemplated heliocentric orbits involved, the use of solar pressure phenomenon is by far the dominant one leading to much shorter spacecraft libration periods and precludes the "inverted" stabilized mode arising from the use of gravity gradient stabilization.

A sketch of the solar pressure-oriented configuration giving the pertinent dimensions and masses is shown in Fig. 11. Considering the configuration with the constants shown to be oriented radially towards the sun by the action of the solar



$r = 25.4 \text{ cm}$	$M_1 = 5672 \text{ grams}$	$I_1 = M_1 \left[\frac{r^2}{4} + \frac{a^2}{12} \right] = 1 \times 10^6 \text{ g cm}^2$
$a = 13.1 \text{ cm}$	$M_2 = 616 \text{ grams}$	$I_2 = M_2 \left[\frac{r^2}{2} + \frac{b^2}{12} \right] = .236 \times 10^6 \text{ g cm}^2$
$b = 27.75 \text{ cm}$	$A = \pi r c = 1.6 \times 10^3 \text{ cm}^2$	$I_{\text{minor}} = I_1 + I_2 = 1.236 \times 10^6 \text{ g cm}^2$
$c = 20.35 \text{ cm}$	$\frac{I_{\text{major}}}{I_{\text{minor}}} = 1.9$	$I_{\text{major}} = I_1 + M_1 L_1^2 + I_2 + M_2 L_2^2 = 2.33 \times 10^6 \text{ g cm}^2$
$L_1 = 4.35 \text{ cm}$		
$L_2 = 40.12 \text{ cm}$		

Figure 11

SOLAR PRESSURE-ORIENTED PAYLOAD

radiation pressure on the vane area A, the equation of motion of such a simple structure is given by:

$$I\ddot{\theta} + f\dot{\theta} + pAl \sin \theta = 0 \quad [10]$$

where

I is the moment of inertia about an axis orthogonal to the boom;

p is the solar radiation pressure and is equal to 4.65×10^{-5} dynes/cm² at 1 A.U.;

A is the effective area of the vane;

l is the mean length of the boom.

Assuming that the viscous damping factor (f) is small, it follows that for small oscillations the period of oscillation of the configuration about a solar radius is:

$$\tau = \frac{2\pi}{\sqrt{pAl}} \quad [11]$$

The result of Eq. [11], which assumes oscillations only in one plane and does not account for any cross-coupling between oscillations about the yaw and pitch axis, is applicable as a "steady state solution," that is, after initial injection transients have subsided. The structure, having a much larger moment of inertia about an axis orthogonal to the initial spin axis and being lossy, will eventually lose its initial spin energy, rendering the spacecraft such that its final oscillatory motion is governed by the results of Eq. [11]. The final libation period of the structure with the constants given is calculated to be

approximately 60 minutes. This can be substantially reduced, if desirable, by the use of a somewhat larger vane area made of lighter material.

C. Power Generation and Control

1. General consideration. The emphasis on the temperature balance and attaining a low equilibrium temperature is not occasioned by a requirement to maintain the electronics at a reasonable temperature value, but from the desire to operate the solar cell arrays at a minimum temperature - maximum power condition. Since there will be a substantial change in the array power output over the orbit due to changes in the temperature-dependent voltage and solar constant-dependent current output, the payload power converter has been designed to sense the voltage and current levels and automatically track the array power profile in a way which allows the array-plus-power converter system to operate at the maximum power point, irrespective of the exact power profile.

2. Solar cell array performance. Based on expected temperatures from the thermal analysis and characteristics of the solar cells, the array performance is that of Table III.

The performance figures shown are based on initial solar cell parameters, undegradated by radiation damage, UV darkening of the cover slides, etc. However, the system power requirements have been designed to allow for a 50 pct reduction in array output which appears to be conservative in that the

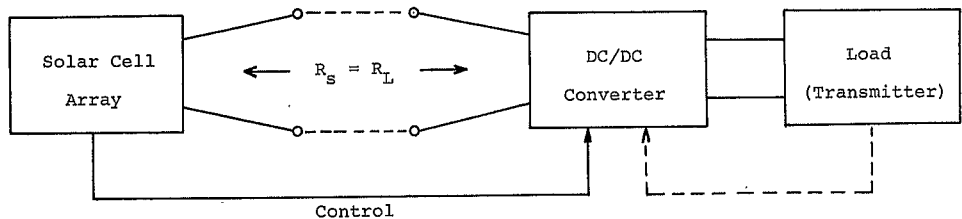
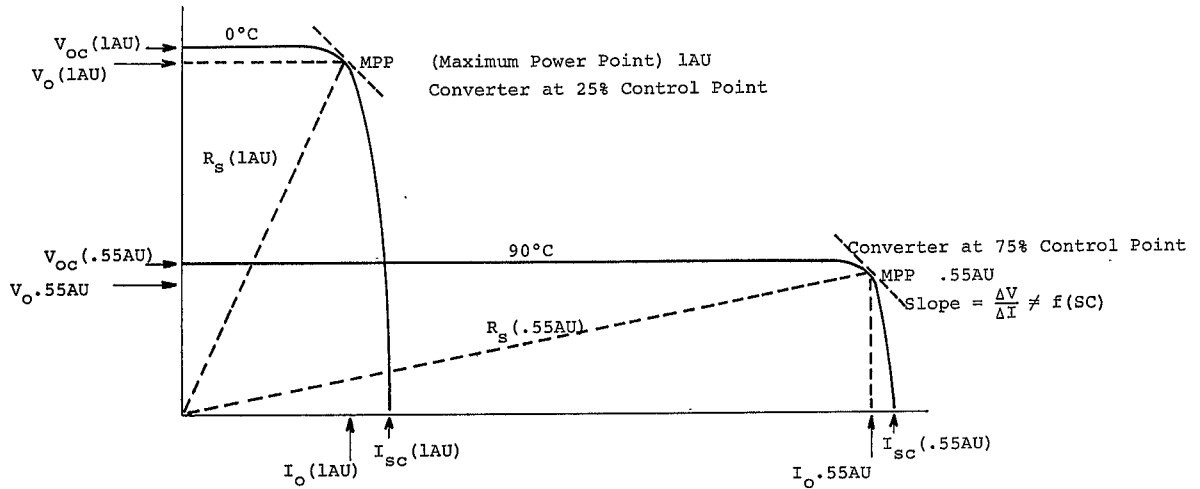
TABLE III Solar Array Performance

1AU				.55AU				
T	V	I	P	T	V	I	P	
260°K	37.4v	.40a	14.9w	370°K	18v	1.60a	29w	Maximum
273°K (10-20)°C	28.0v	.405a	11.32w (25%)	380°K (90-100)°C	16.3v	1.65a	26.9w (75%)	Nominal
283°K	26.6v	.41a	10.8w	400°K	13.4v	1.70a	22.9w	
290°K	24.6v	.415a	10.2w	420°K	10.5v	1.80a	19w	Minimum

expected power decrease is estimated to be less than 25 pct over a two-year period. In addition, the degradation estimates are based on constant temperature profiles (temperature as a function of solar constant) which is in itself conservative in that the major degradation is expected to be due to cover slide UV darkening which would tend to make the array run somewhat cooler by virtue of the lower absorbtivity (higher reflectivity) of the darkened slides.

To protect against catastrophic failure the total array has been segmented into eight parallel sections which operate independently.

3. DC-to-DC power converter. The 1 A.U. and 0.5 A.U. solar cell array, voltage-current profile based on the expected spacecraft array temperature is shown in Fig. 12. A salient feature of this profile is that, as the temperature increases and consequently the voltage decreases as a result of the increasing solar constant toward perihelion, the array output power increases even though the voltage is dropping because of the increased current output. This simultaneously decreasing-voltage, increasing-current profile causes the array source impedance, which the power converter input impedance must "match" for maximum power transfer, to decrease radically (by about a factor of eight for the conditions shown) in a manner which is difficult to predict with prerequisite information. In order to take advantage of the power "climb" toward perihelion, the DC-to-DC converter is



POWER GENERATION AND CONTROL

Figure 12

designed to adjust its input impedance to a value equal to the array output impedance by sampling the array voltage-current slope near the maximum power point (MPP). The manner in which this is accomplished is shown in Fig. 13.

Briefly, the transistor T_1 which is driven by a square wave oscillator functions as an alternate open-closed switch thereby shutting a known value resistor (R^*) across the array. The "dither current" (ΔI) drawn through R^* results in an array voltage drop of ΔV which in turn is a function of the array $V - I$ characteristics at the MPP. The magnitude of ΔV is converted to a DC voltage (through D_1 and C_1) and used to control the DC-to-DC converter so it accepts that value of current which the solar cell array is capable of delivering. In the above manner maximum power transfer from the solar cell array to the power converter is assured.

The essentials of power processing within the converter are shown in Figs. 14 and 15. Basically, the converter is constructed from "building-block converter units," each unit handling a fraction of the total power. As the power profile climbs (or decreases as the case may be), units are effectively added (or subtracted) in a duty-cycled (percent of the time) fashion. This method not only affords a flexible power-generation profile but allows for each basic converter unit to be designed for near full power, or off, operation, and hence, maximum efficiency is realized as well as redundancy against failure without weight penalty; since the major part of the converter weight is associated with

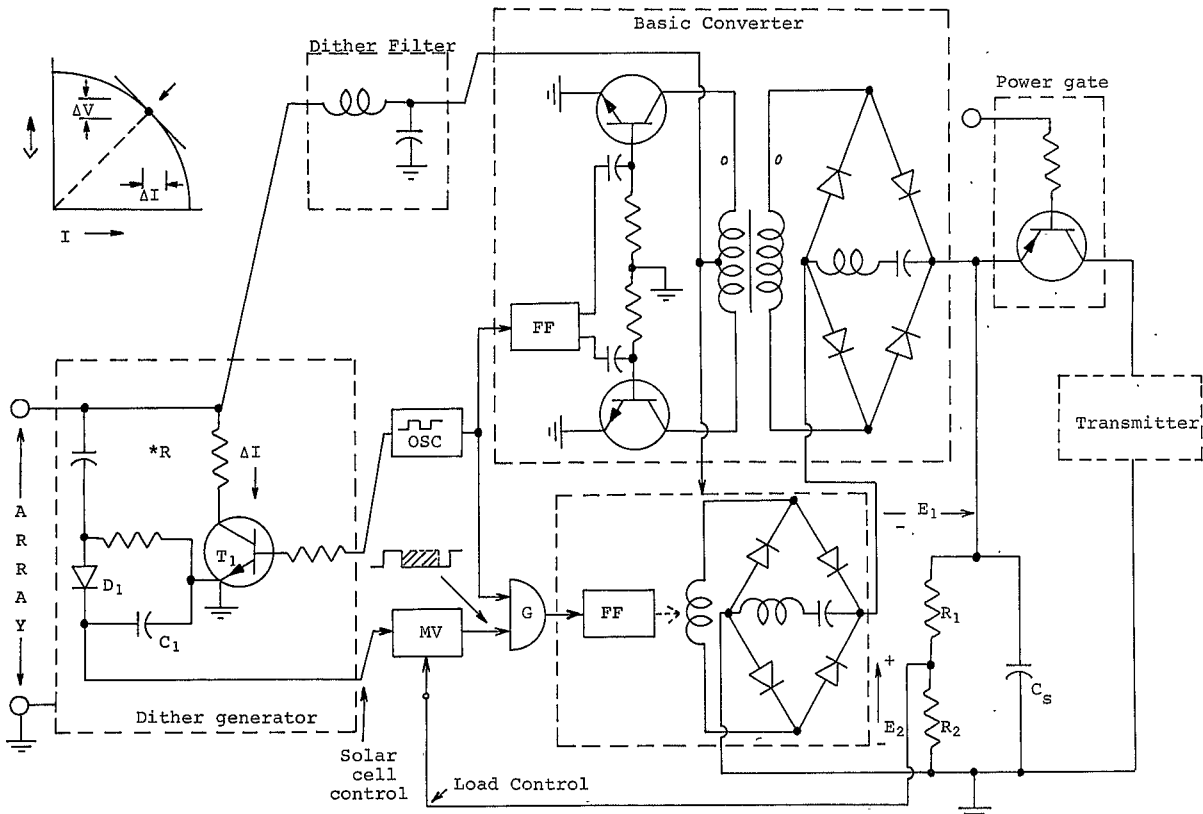


Figure 13 MAXIMUM POWER POINT CONVERTER

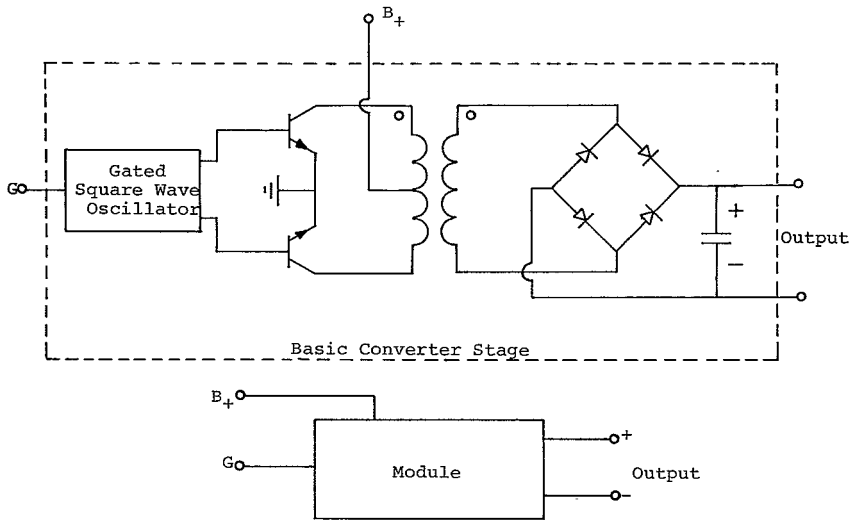


Figure 14
POWER CONVERTER

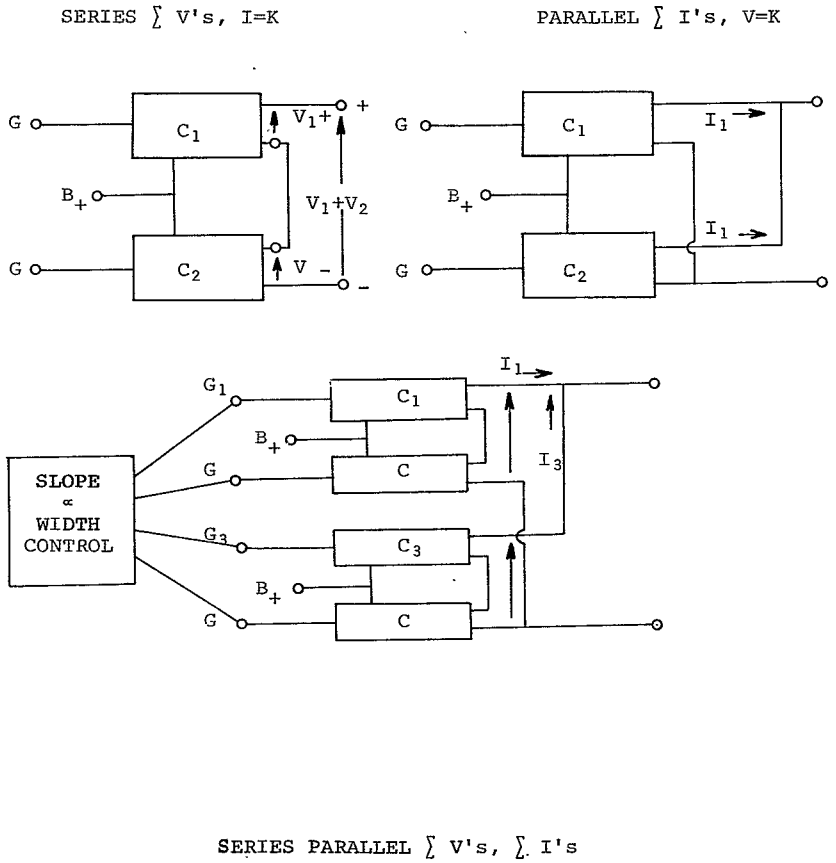


Figure 15 MAXIMUM EFFICIENCY POWER CONVERTER

the mass, i.e., power-handling capabilities of the transformers which is essentially equal whether the mass (power) is concentrated into one transformer or distributed among several.

In order to take advantage of the additional power available when the spacecraft is not at or near aphelion, the output voltage of the power converter is caused to increase and the transmitter operating at a higher collector voltage (relative to the value at 1 A.U.) delivers additional power. The feedback path composed of R_1 and R_2 (Fig. 13) serves to limit the converter output voltage to a maximum value less than the transmitter design limit.

The solid state transmitter described in Fig. 16, like the converter, incorporates the modular conception, the total power being derived by "RF summing" the outputs of many basic RF amplifier units. Each RF power amplifier is individually fused to the DC power converter with fuses whose burnout characteristics are dependent upon average current. For pulsed load systems made up of a number of individual loads, the required fuse characteristics are readily attainable. In the event of an amplifier failure (a short), the entire power-converter output is drawn by a single fuse whose power-handling capacity may be made small by virtue of having many loads involved. Pulsed loads are, in general, easier to fuse owing to the inherent internal time constant associated with fused burnout.

4. DC energy-storage considerations. A high-peak power system has many advantages such as ease of detectability and sim-

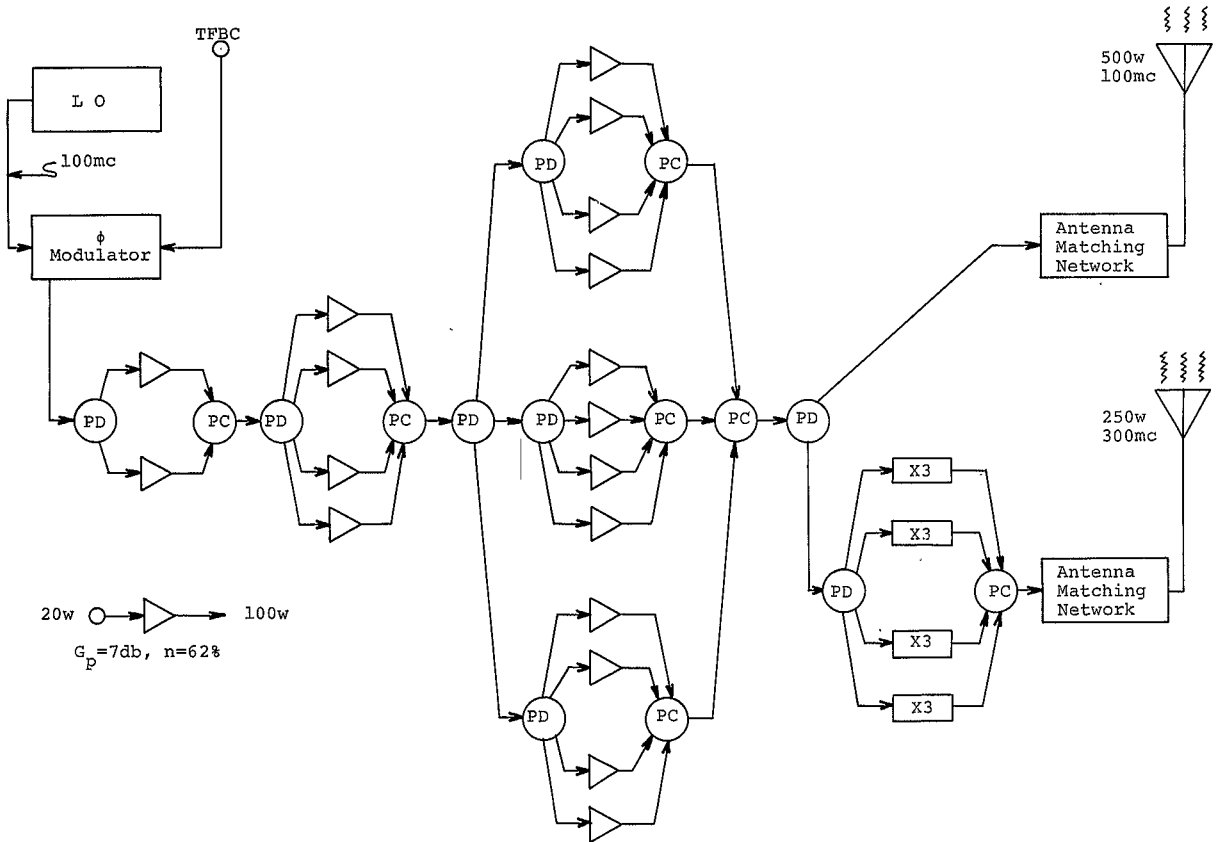


Figure 16. TRANSMITTER CONFIGURATION

plification of on-board data processing systems. However, the required energy storage system has, in the past, confined the application of high-peak systems to areas where mass is not an important system consideration. Although the Sunblazer payload is mass limited, there are two energy-storage systems that appear compatible to the overall system configuration. System trade-offs for both an electrical energy-storage system using capacitors and a chemical energy-storage system using nickel-cadmium cells are being investigated.

Commercially available capacitors have nominal capacitance per unit mass ratios of up to 5,000 μf per pound. Aluminum electrolytic devices which have the most favorable capacitance-to-mass ratio will store 25 joules of energy/lb at 100 volts DC. Only a portion of this energy is available, depending upon the degree of voltage degradation permitted during pulse discharge. For a 30 pct drop in voltage, about one-half of the stored energy is available to the transmitter.

The efficiency of such a capacitor energy-storage system is high. Because of the initial voltage on the capacitor during the charging cycle, the charging efficiency η of the system is approximately

$$\eta = 1/2 \left[1 + \frac{E_0}{E} \right] \quad [12]$$

where E_0 is the initial voltage on the capacitor and E is open-circuit output voltage of the DC-to-DC converter. In the case of 100-volt converter voltage and a 30 pct drop in voltage during the pulse, the capacitor-charging efficiency is 85 pct. A further

increase in charging efficiency is attainable, at the expense of system complexity, by shaping the converter output voltage to minimize the energy loss during the charging period.

Aluminum electrolytic capacitors have a long history of reliable operation in unattended field sites. However, their use in the expected space applications demands that a component testing program be conducted. Vacuum tests have been in process for several months and no loss of weight due to electrolytic evaporation or seal failure has been observed.

A battery system is an attractive alternate to the capacitor system because of the very high ratio of stored energy per unit mass. In the case of nickel-cadmium cells, about 3×10^4 joules of energy per pound may be stored. Again, these devices have a long reliability history and have been used extensively in spacecraft applications.

For the Sunblazer transmitter, a battery system has two major limitations: (1) low voltage per cell, and (2) high internal impedance. The low per-cell voltage requires the use of a long series string of cells to obtain the 100-volt transmitter operating voltage. The high internal impedance limits the discharge efficiency and the rate at which the energy may be absorbed by the transmitter.

A comparison of contemporary battery design with capacitor systems indicated that the capacitor system was superior in regard to reliability and weight. Thus the prototype was constructed using a capacitor system for energy storage.

D. RF Electronics

1. General system considerations. In connection with the Sunblazer payload, the high power RF pulser serves both as a telemetry transmitter and an experiment transducer. The operating frequency, output power, and pulse profiles are dictated by system considerations related to both of these transmitter functions, especially through the expected carrier delay, DC power and storage, and the available spacecraft volume and weight. To satisfy the requirements of the propagation experiment, a system life of two years is a necessity. From an overall system point of view, the peak radiated output power per unit mass is a basic figure of merit.

In principle there are no fundamental device limitations imposed by the power or frequency of the transmitter in that solid state devices are available which will generate substantial power, either pulsed or C.W., in the microwave frequency range. Theoretically, any power level may be obtained by paralleling a number of devices. However, problems relating to device-parameter matching, circuit-impedance levels, and parasitic elements limit to approximately four the number of devices that may be directly paralleled with a high degree of reliability.

By incorporating redundancy into the system design, increased transmitter performance and reliability may be achieved. For example, at the "microcircuit" level many transistors may be fabricated on one substrate and, either by careful selection and direct paralleling or through the use of distributed parameter-combining networks, many units may be effectively paralleled,

making one large area (high-power) device. On the circuit level, higher power may be obtained by utilizing several devices in parallel, forming one amplifier circuit; and on the subsystem level many amplifiers may be combined. Thus, a high-power transmitter may be designed using a distributed-component concept on every level from devices through systems.

An important feature of a distributed-component system is that a failure of one of the components does not, in general, cause a system failure, but rather a slight degradation in system performance. Therefore, a redundant system may be designed to "die gracefully," thereby greatly increasing the expected useful system life.

In this spacecraft electronic system, the peak RF power is important as well as the expected system life. The system need for high peak power at moderate average power levels alleviates the use of massive transistor packages and heat sinks. The peak power-handling capability of transistors which are not directly related to operating duty cycle over a very wide range of duty cycles, pulse repetition frequencies, and pulse widths, typically produce 3 db to 6 db more power in the pulsed mode than in C.W. operation. Higher than 6 db peak to C.W. power ratios are not, in general, attainable due to physical imitations imposed by device parameters, principally current crowding, secondary voltage breakdown, and thermal time constants associated with the semiconductor wafer.

2. System description. A prototype high peak-power transmitter was designed and constructed to demonstrate the feasibility of a redundant low-mass, pulsed RF system. The design consisted of a cascade of a low-level crystal oscillator, multiplier stage, a phase modulator, driver amplifier, and power amplifiers. Typical 100 MC system operating conditions were: 400 watts of pulsed output power, once a second at a pulse width of 2.42 ms. Two hundred watts of RF power were available at 100 MC, and 200 watts of power were used to drive a frequency-multiplier circuit. In the discussion that follows, the power-output stages will be discussed first and the low-power driver stages last.

A block diagram of the prototype pulse transmitter is given in Fig. 17. The basic building block is a 100 MC, 100 watt output, saturated class C amplifier operating at 62 pct collector efficiency and 7 db gain. The amplifier rise time was 2 μ s, and the peak collector current was 1.6 amps at 100 volts DC. Each amplifier consists of an input-matching network, two transistors in parallel, and an output-matching network as shown in Fig. 18. Four of these amplifiers are driven from one basic 100-watt circuit through an LC power-divider network. The 100-watt amplifier is in turn driven by low-level, high-gain stages.

In the prototype transmitter, conventional packaging techniques were used. The specific power ratio of the complete transmitter was 1.8 watts/gram. A miniaturized version of the 100-watt amplifier weighing 12 grams and occupying 1.56 in² of

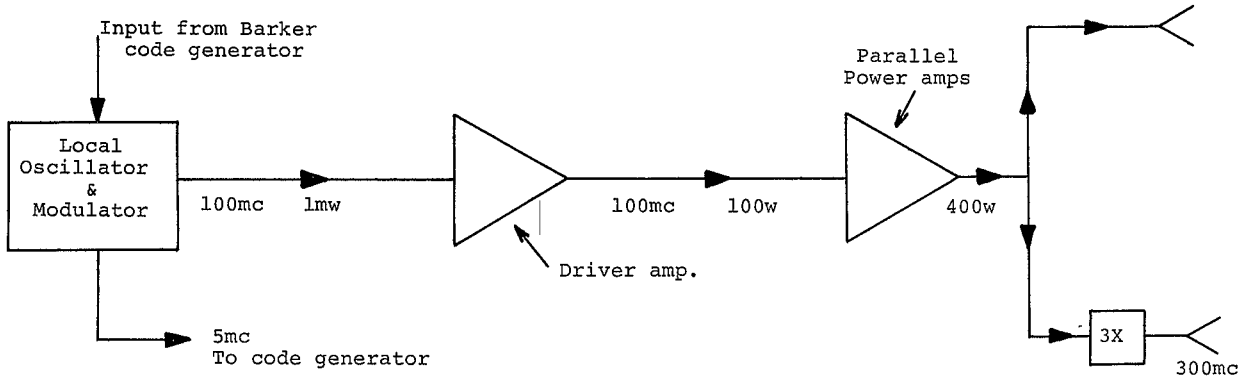


Figure 17 TRANSMITTER BLOCK DIAGRAM

area was constructed. As a further development, four 100-watt amplifiers were constructed on one printed circuit board along with the basic power dividing and combining circuits. The object was to construct a basic building block 400-watt amplifier for the one kw flight transmitter.

The attainment of high peak powers depends to a great extent on the degree of circuit level redundancy used in the transmitter design. Since the use of power divider and combiner networks is a central part of the system design, a consideration of these filter characteristics follows.

An L section is shown in Fig. 19 along with the definition of the pertinent impedances associated with the matching network. For simplicity, the generator and load impedances Z_g and Z_L have been chosen as pure resistances so that "lossless" matching may be accomplished by pure reactances, and for the case shown in the figure, Z_g is chosen to be greater than Z_L . On a generalized basis, Z_s must be in series with the lower impedance, either Z_L or Z_g . The matching reactances are related to the generator impedance Z_g and the load impedance Z_L by the following set of equations:

$$Z_s = \pm j \sqrt{Z_L (Z_g - Z_L)} \quad [13a]$$

$$Z_p = \mp Z_g \sqrt{(Z_L) / (Z_g - Z_L)} \quad [13b]$$

To maintain the matching conditions, the reactances Z_p and Z_s

BASIC 100W AMPLIFIER

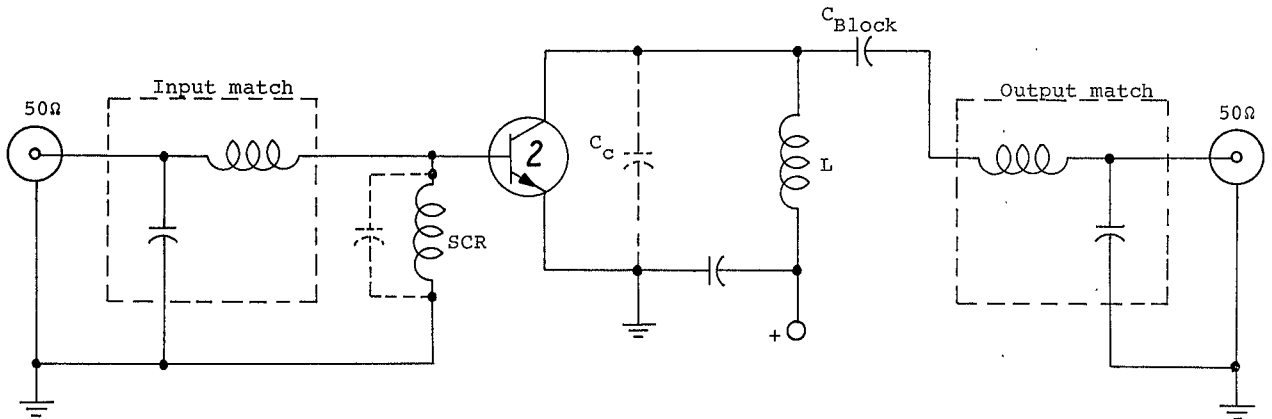


Figure 18

BASIC 100W AMPLIFIER

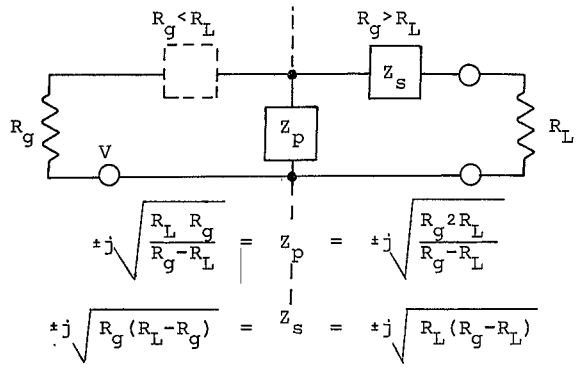


Figure 19

L SECTION IMPEDANCE MATCHING

must be opposite sign, and for high-power class C amplifiers a low-pass realization is usually employed because of its filtering characteristics.

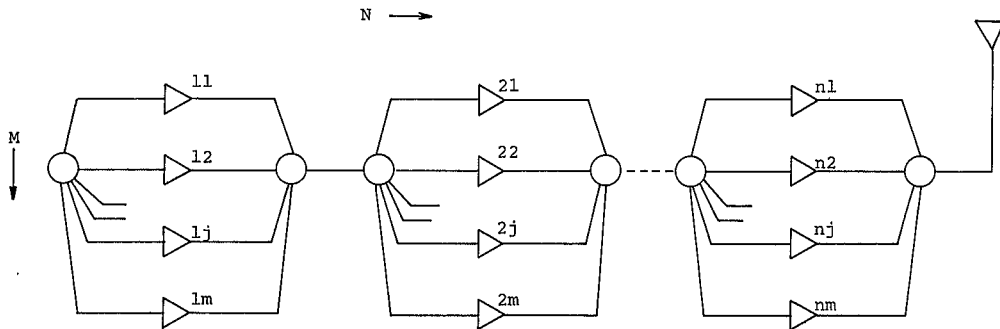
When N identical amplifiers are to be driven from one source of internal resistance R_g , modified L sections are used. For common emitter amplifiers, a low-pass L section is designed to match r_b , the approximate input impedance of the amplifier, to a resistance of $N R_g$. The inputs of the N sections are common, and when each inductor L is properly loaded, the input impedance is R_g .

The most probable device failure is a short in either or both of the semiconductor junctions. For the case of a short from base to emitter, the series inductance of one section of the power divider is in parallel with the input capacitor. The L section becomes approximately parallel resonant with a result that the input to the power divider is slightly mismatched. In the case of a device-open circuit, a reactive term appears in the input impedance-to-divider, causing only a slightly greater mismatch than for a short circuit failure.

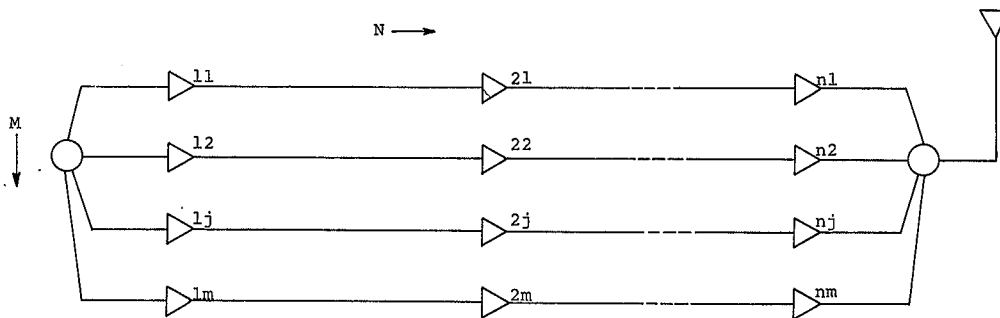
Considering a cascade of N amplifiers, there are M identical amplifier rows as shown in Fig. 20. In the case of a failure it can be shown that an improvement factor F , which is the ratio of output power in the case of circuit redundancy to the output power without redundancy, is given by:

$$F = \frac{2M^2}{2M^2 - 2M + 1} \quad [14]$$

where $M = 1, 2, 3, 4$.



a. REDUNDANT POWER AMPLIFIERS



b. NON-REDUNDANT POWER AMPLIFIERS

Figure 20

For $M = 4$, an improvement of 28 pct is feasible.

An amplifier-life test program is being conducted to evaluate experimentally some of the circuit concepts outlined above. A 500-watt pulse amplifier is used with outputs of seven 75-watt amplifiers combined by modified L sections. Each amplifier has two devices in parallel. Tests have been conducted over a wide range of pulse conditions and over 3,000 hours of failure-free amplifier life have been obtained to date.

3. Basic amplifier balance and distortion. Because class C amplifiers are operated in a saturated condition, distortion of the RF spectrum must be considered. Evaluation of this distortion was obtained by utilizing a C.W. rather than pulsed operation to determine the extent of spectrum deterioration. A high-level carrier, phase-modulated by a 50 kc square wave, was used to drive a class C amplifier circuit under collector conditions typical of saturated-pulse operation. No discernible distortion or unbalance was detected in the amplitude for the first three Fourier components centered around the carrier.

A more important source of spectrum distortion results from the required amplitude and phase balance between parallel-power amplifiers and power-divider networks and, in order to obtain the necessary balance, the amplifier input circuits were matched, using equivalent half wavelength sections of coaxial transmission line. This eliminated the spurious effects of power-monitoring devices that were connected at the input networks

in order to measure and balance the power amplifiers and divider networks. A somewhat novel measurement technique, using pulsed Lissajous patterns at 100 MC, has been developed to show balance characteristics.

After the transmitter is aligned, a system measurement at 100 MC was made, and results indicate that the bandwidth of the 100 MC portion of the transmitter is adequate to "readily pass" the Barker code modulation of the carrier.

4. Varactor multiplier

a. General considerations. In order to generate the delay experiment reference signal at 300 MC, a varactor-type frequency tripler is used. This approach was chosen because conversion efficiencies of 60 to 65 pct are attainable at the one kw input power level. In addition, these circuits are not unduly complicated nor difficult to align and no external DC power input is required.

Both pulsed and C.W. tripler have been built and evaluated. The basic pulsed tripler uses two 100-watt power varactors in series in order to accommodate input powers of 200 w. The C.W. type was constructed, using heat sinks, and was capable of handling C.W. input powers as high as 100 w. Most of the experimental evaluation work was done using the C.W. multiplier in order to simplify the measurement procedures.

b. Pulsed 100 MC tripler. A block diagram of the 100 MC pulsed-varactor frequency tripler is given in Fig. 21. Impedance matching is provided at both input and output by means

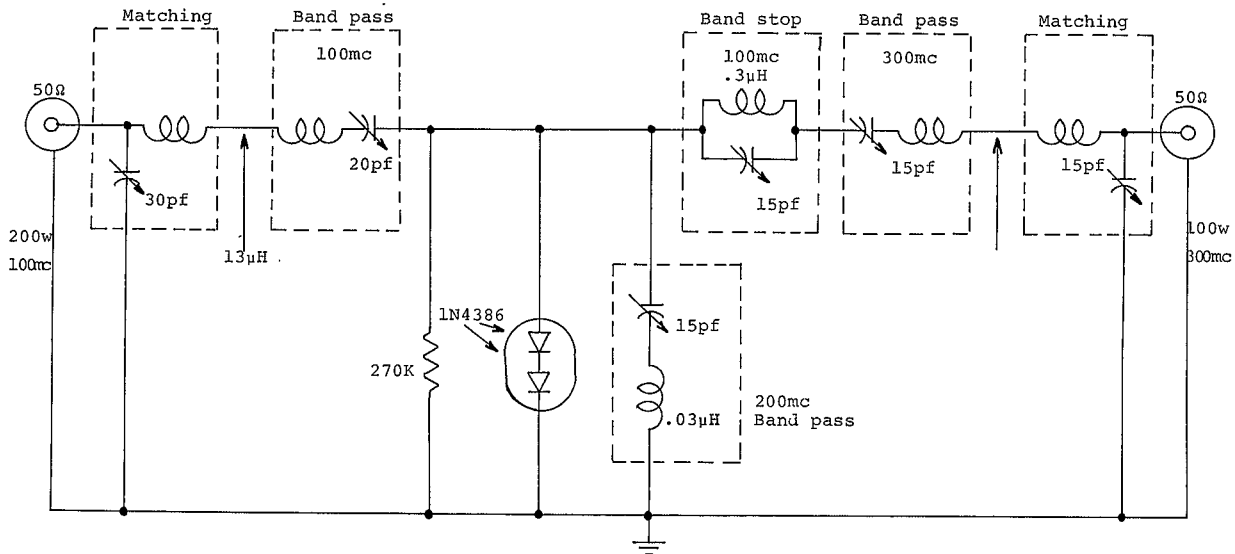


Figure 21. BASIC POWER TRIPLER

of L matching sections. Series resonant circuits are provided at 100, 200, and 300 MC to obtain efficient varactor operation. While the type of varactor used in this circuit (a charge storage type) may be operated without the 200 MC circuit, the addition of this idler circuit increases operating efficiency. Parallel traps are also included to prevent energy feed-through at both 100 MC and 300 MC.

This circuit operated at 50 pct efficiency. The 300 MC output waveform was considerably distorted, due to inadequate output-signal filtering. This condition was corrected, and circuit efficiency has been increased through evaluation conducted with design studies of the C.W. multipliers described in the next section.

c. C.W. tripler. The 100 MC, C.W. tripler is essentially the same design as the pulsed tripler, with the exception that the 100 MC parallel resonant trap has been replaced by an external narrow bandpass filter composed of a pair of loosely-coupled paralleled-tuned tank circuits, giving a 3 db bandwidth of 40 MC and 70 db fundamental harmonic suppression. A similar filter, designed for a center frequency of 100 MC, was used in the input line to prevent harmonic feedback to the source.

Several devices were evaluated in this C.W. operating mode. Input power was varied from 10 watts to 180 watts. Typical operation efficiency was 62 pct, but efficiencies as high as 80 pct and as low as 35 pct were observed. It appears from

the experimental data that efficiencies of between 60 to 65 pct are routinely attainable with these circuit techniques.

The spectral characteristics of the output waveform were measured on a spectrum analyzer. The tripler was operated at an input level of 90 w and the relative levels of the various harmonics measured. The second harmonic was 30 db below the carrier level and all other harmonics were at least 50 db below the carrier.

In order to investigate the phase modulation characteristics of a tripler circuit, a 100 w, 100 MC signal phase modulated at a 50 kc rate was used to drive the multiplier. Fig. 22 shows the spectrum of this input signal, and the other seven photographs of Figs. 23, 24, and 25 show the output of the multiplier at various harmonics. All of the odd harmonics contain modulation signals of the input spectrum while none of the even harmonics have information content. This result is in agreement with two different analyses, the first of which was based on the assumption that the varactor is a square law device and the second on the assumption that the diode operates as a step-recovery device.

Attempts at a purely analytical solution for a high-power multiplier have not been successful, but an approximate empirical design technique has been obtained. It has been possible, however, to show that the design calculations for the input, output, and idler networks may be carried out independently. Although these networks connect to the same point, the relative impedances are such that negligible interaction results.

Figure 22

50KC Square Wave through
Variactor Tripler.

Output of Tripler at
Various Harmonic Frequencies.

a) $f=100MC$

b) $f=200MC$

c) $f=300MC$

Figure 23

d) $f=400\text{MC}$

e) $f=500\text{MC}$

f) $f=600\text{MC}$

Figure 24

g) $f=700\text{MC}$

h) $f=800\text{MC}$

Figure 25

3 Folds of Barker Code
through Varactor Tripler.

a) $f=100\text{MC}$

b) $f=200\text{MC}$

c) $f=300\text{MC}$

5. Low-power transmitter circuits. The low-power driver circuits described below are constructed on a single printed circuit card. Two synchronous outputs are provided, one output at 100 MC to drive the high-power amplifiers, the other at 5 MC as the master clock for the system. For the Sunblazer experiment, long-term crystal oscillator drifts may be compensated at the receiver. However, the desired short-term stability of one part in 10^8 requires on-board temperature control.

The circuitry used in the low-level stages is of conventional design except that for the 5X multiplier a "snap diode" harmonic generator is used. A block diagram of the low-level portion of the transmitter is given in Fig. 26. The output of a 5 MC crystal oscillator is fed to both a clipper amplifier, which supplies the master clock for the digital circuitry, and to a conventional class C transistor-frequency multiplier.

In cascade with the transistor multiplier (X4) is a 5X "snap diode" frequency multiplier. This two-stage multiplication process was selected because of good stability and spectral purity of the 100 MC carrier. The "snap diode" output signal is amplified in a conventional class A circuit which drives a balanced diode bridge modulator. The output of the modulator is approximately 0.4 mw and drives the high-power driver amplifiers.

6. Barker code modulation characteristics. In the delay experiment accurate time resolution is obtained by means of a pulse-compression technique. In this system biphase modu-

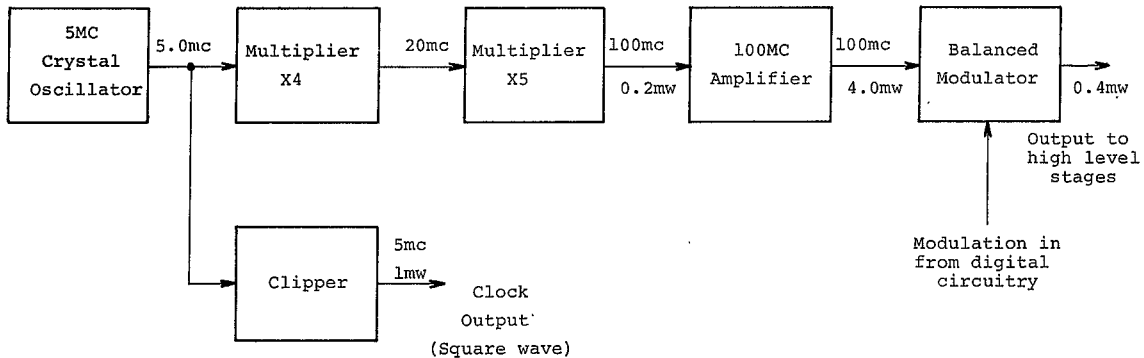


Figure 26 LOW LEVEL TRANSMITTER STAGES
 BLOCK DIAGRAM

lation, which tends to broaden the spectrum of the transmitted pulse, is encoded onto the carrier by means of a balanced diode bridge circuit. The basic code is composed of 20 μ s pulses, transmitted in an 11-bit Barker sequence. A bridge modulator advances the phase of the carrier 180° at each transition point of the Barker sequence. The effectiveness of the pulse compression is limited by the distortion introduced in the power amplifiers. For this reason, both the power-amplifier circuits and the frequency-multiplier circuits were evaluated to determine their effect on the modulated carrier.

Before examining the Barker code in detail, consider the case of a continuous carrier at frequency ω_0 modulated by the function $A(t)$. The output of the modulator may be expressed as $f(t)$ where:

$$f(t) = A(t) \cos \omega_0 t \quad [15]$$

The Fourier transform of $f(t)$, which is the spectrum of the square wave $A(t)$ centered about the carrier, is suppressed and sidebands occur separated in frequency by multiples of the repetition rate of the modulating square wave.

Although there are some basic similarities, because of the pseudo-random nature of the Barker code, its spectrum is more complex than that of a simple 20 μ s square wave. Since the Barker sequence has a non-zero time average, the carrier will not be completely suppressed, and a characteristic 50 kc period to the spectrum exists. The complete 26 ms transmission contains

fine structure down to 40 cycles/sec. Photographs showing these characteristics, as measured, along with a computer plot of a Barker code spectrum are given in Figs. 27 and 28.

7. Antenna design. The antenna system of the Sunblazer prototype payload is composed of two center-fed quarter wavelength radiating elements and matching sections at each frequency. The transmitter output is connected to the radiating elements through phasing cables and attenuators which are used to protect the high-power transmitter amplifiers from an accidental mismatch and to reduce the radiant RF power to a level compatible with the input sensitivity of our prototype system test receivers.

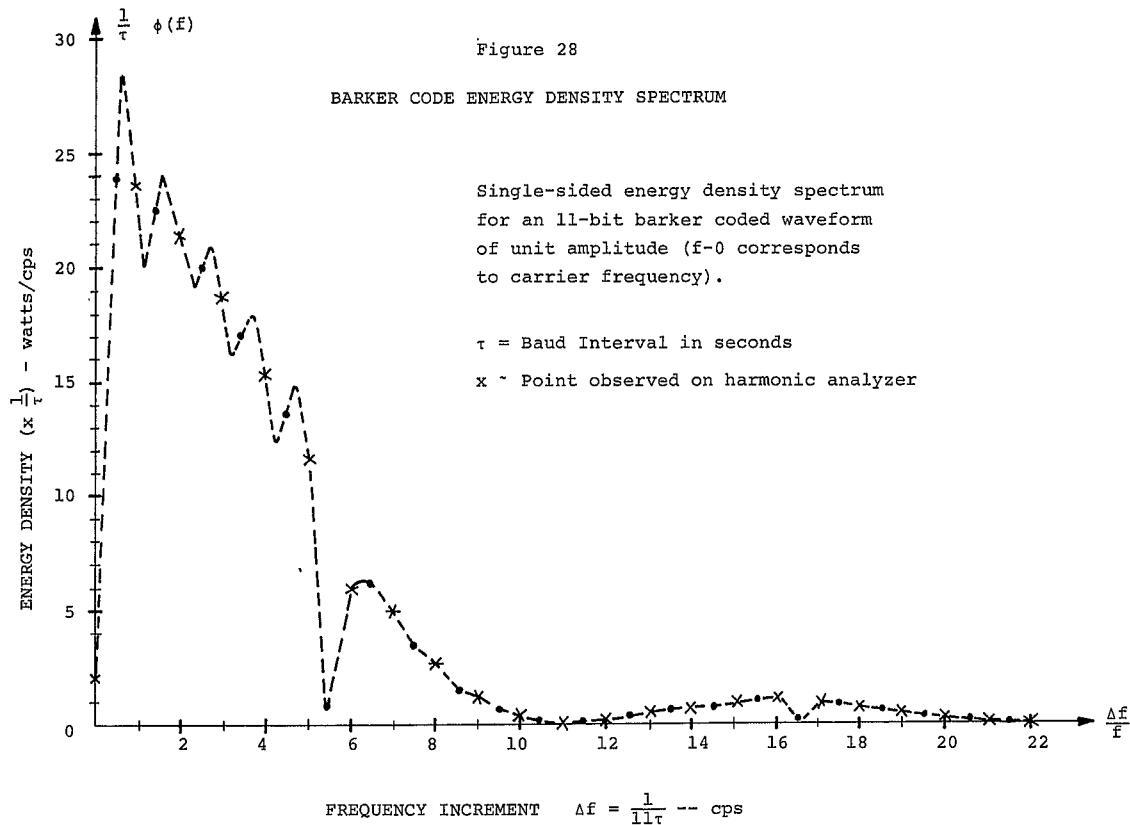
The two dipole antenna pairs are mutually orthogonal and perpendicularly centered about the longitudinal axis of the spacecraft. Because of payload symmetry, the maximum radiation occurs along its longitudinal axis, and the radiation pattern has a minimum in the plane which contains the radiating elements.

Several other antenna array systems are also being investigated. The most promising array is a cascade of transposed half wavelength, coaxial transmission line sections. This system would require 3-axis stabilization but would greatly enhance the signal-to-noise ratio.

E. Barker Code Generator

1. The Barker code. In order to perform the differential time measurement, the signal being transmitted must have high resolution, low ambiguity, and a high probability of detection. The latter is a direct function of the signal energy while

Figure 27
Repetitive Spectrum of Single Fold of Barker Code
12kc/div.



the former are functions of signal bandwidth and spectral characteristics. The Barker code chosen is one of a class of codes in which these desirable characteristics exist.

Matched-filter techniques are used in order to detect the Barker code. This filter is an N-port linear element that has a transfer function equal to the complex conjugate of the signal to be received.

Generally the response of a linear filter, having a transfer function $h(\tau)$, to an input signal $s(t)$ is given by:

$$y(t) = \int_{-\infty}^{\infty} h(\tau) s(t-\tau) d\tau \quad [16]$$

Specifically, if $h(\tau) = s(-\tau)$, the condition for a matched filter, this becomes:

$$y(t) = \int_{-\infty}^{\infty} s(-\tau) s(t-\tau) d\tau \quad [17]$$

This function is shown in Fig. 29 for the Barker coded signal which is depicted by Fig. 30. The Barker code, properly detected, has a unique central peak that is significantly larger than any of the sidelobes. This response has little ambiguity; that is, there are no other peaks that would cause false triggering of the threshold detector located at the filter output.

The amplitude of the peak is obtained by substituting a value for t equal to zero into Eq. [17], resulting in:

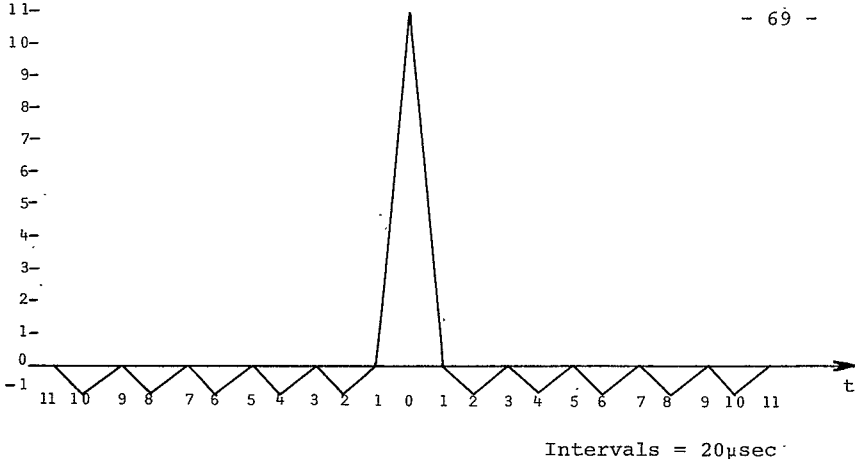


Figure 29 - MATCHED-FILTER RESPONSE TO A BARKER CODED INPUT SIGNAL

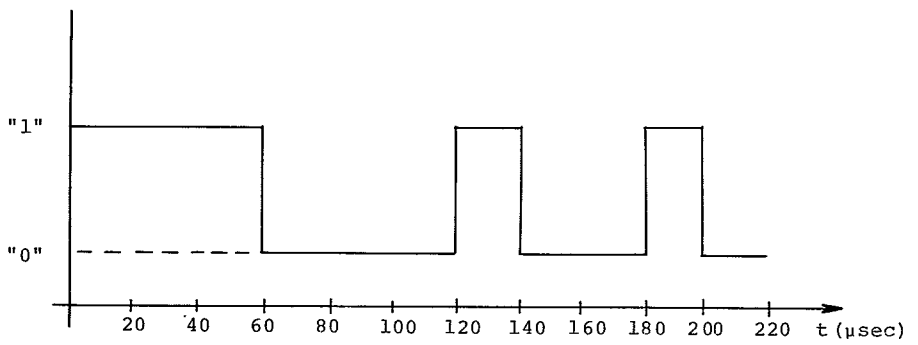


Figure 30 - AN ELEVEN-BIT BARKER CODE

$$y(0) = \int_{-\infty}^{\infty} s^2(\tau) d\tau \equiv E \quad [18]$$

This equation is identical to the signal energy. Thus, it is seen that this code and its complementing matched filter compress the signal energy into a central, well-defined pulse containing nearly all of the signal energy. The pulse is M units high, corresponding to the M units of energy within the Barker code, and its width is the reciprocal of the code bandwidth (50 kc).

In order to insure good detectability when the transmitter is peak-power limited (i.e., when the energy per bit is constrained at some maximum), M must be made very large. Unfortunately, the longest known Barker code contains only 11 bits, and in order to overcome this limitation a technique of folding the code within itself is used. This technique, which does not increase the pulse peak-to-sidelobe ratio (fundamentally limited at 11:1), does, however, enhance the signal, thereby increasing overall detection probability.

A triple-folded Barker code is depicted in Fig. 31. The matched-filter response to such a signal is similar to that of Fig. 29, the central peak being 1331 units high, corresponding to the number of bits in three folds of the Barker code. The sidelobes are 121 units high, thereby corresponding to a peak-to-sidelobe ratio of 11:1. The important contribution of this technique is that it raises the signal above the background noise by

MAIN TELEMETRY FORMAT

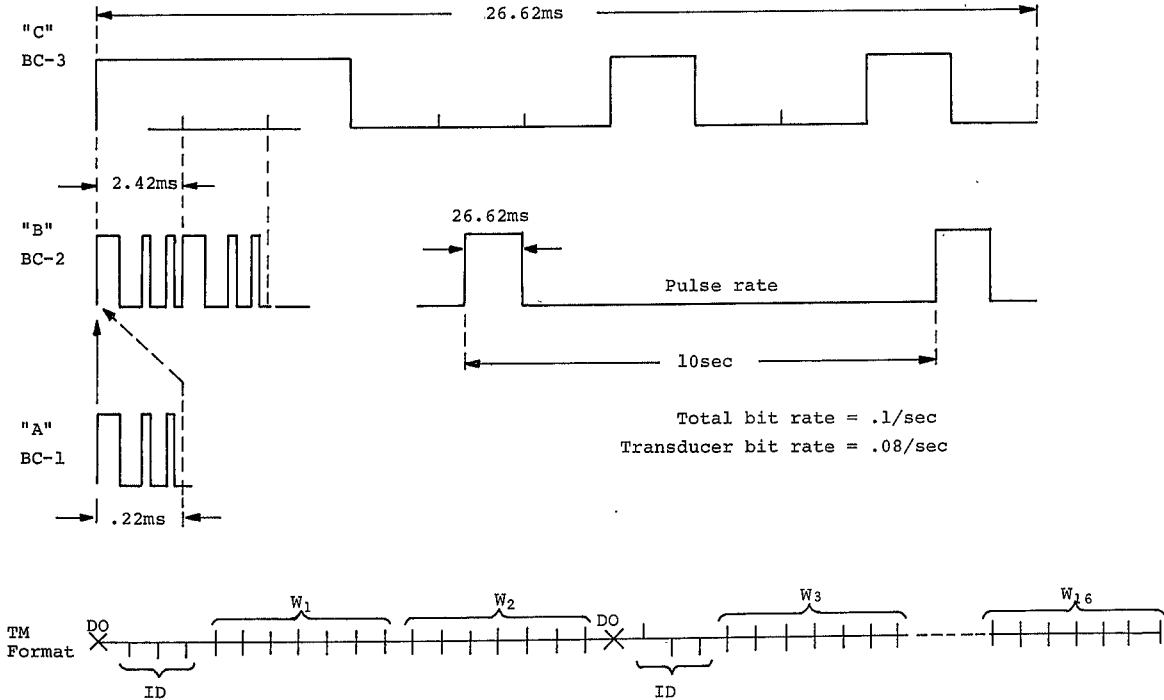


Figure 31 TRIPLE-FOLDED BARKER CODE

permitting the energy of the central peak to be several orders of magnitude higher than is possible with only one fold which permits detection of the signal in the presence of severe noise limitations.

2. Barker code generator. The circuitry that generates the triple-folded Barker code is shown in Fig. 32, where outputs A, B, and C correspond to the waveforms shown in Fig. 31. This coder consists of three sets of 11-bit feedback counters, each generating the waveforms for the respective fold of the code. That is, the first counter and its associated gating generates the envelope of the first fold, while the second and third counters generate the waveforms of the next two folds respectively.

Each envelope would normally drive a phase-shifting network within the modulator electronics. In particular, when the first envelope was at an "0" level, the signal would be shifted by 180° ; alternately when this envelope was at a "1" level, the signal would be shifted by 0° . This signal would then be introduced into the second-phase shifter which would add either 0° or 180° of phase shift depending on the logical level of the second fold controlling it. The third network would similarly be controlled by the third envelope.

A "truth table" listing the eight logical combinations of phase reversal that are possible is given by Table IV. The required envelope follows the additive rules of Boolean algebra which corresponds exactly with binary addition. Therefore, the envelopes generated by the gating associated with each feedback

Table IV *

A. Phase Coding				B. Binary Equivalent			
<u>Fold 1</u>	<u>Fold 2</u>	<u>Fold 3</u>	<u>Sum</u>	<u>1</u>	<u>2</u>	<u>3</u>	<u>Sum</u>
1. 0 °	0 °	0 °	0 °	1	1	1	1.
2. 180°	0 °	0 °	180°	0	1	1	0
3. 0 °	180°	0 °	180°	1	0	1	0
4. 180°	180°	0 °	360°=0°	0	0	1	1
5. 0 °	0 °	180°	180°	1	1	0	0
6. 180°	0 °	180°	360°=0°	0	1	0	1
7. 0 °	180°	180°	360°=0°	1	0	0	1
8. 180°	180°	180°	540°=180°	0	0	0	0

* The equivalence between the two tables is apparent when the substitution "1"=0° and "0"=180° is made.

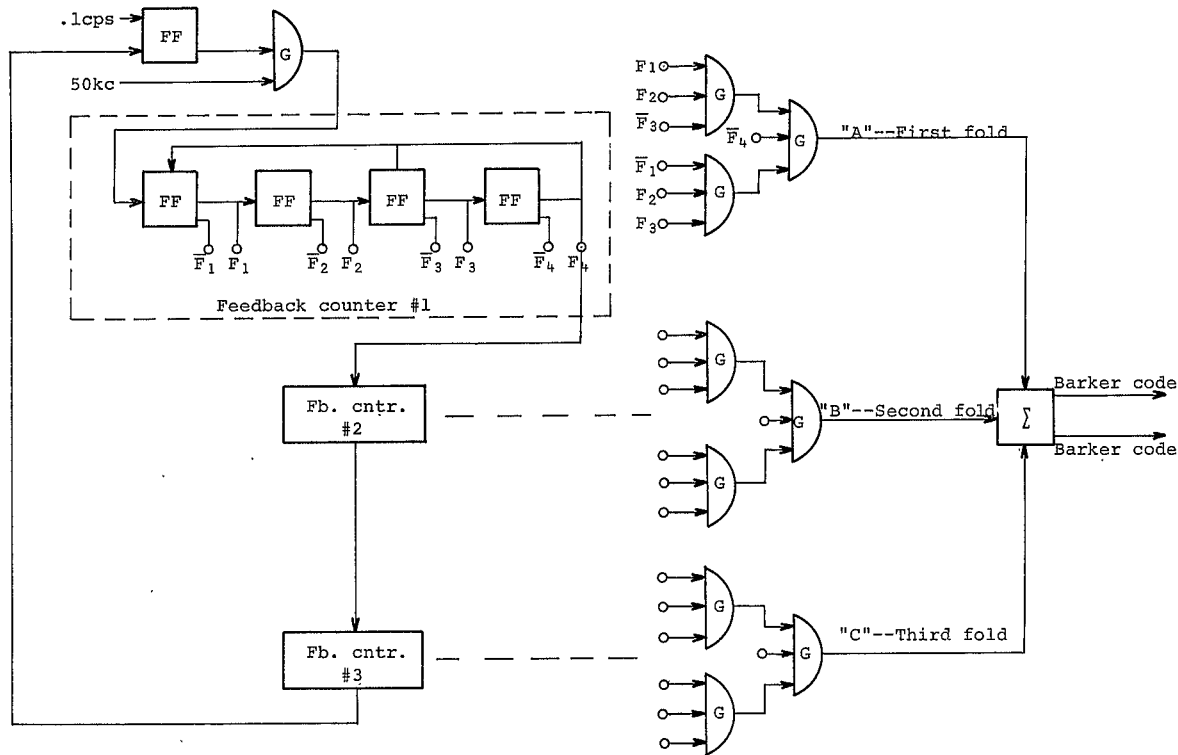


Figure 32 BARKER CODE GENERATOR

counter are logically added by means of a "binary summer." The output from this circuit is the triple-folded Barker code and is used to modulate the 100 MC, RF carrier.

The gate at the input to the first counter is actuated at the beginning of the transmission period, which is generated from high precision, crystal frequency. The gate remains open until the last bit of the code is generated, which occurs after 1331 input pulses have been counted. Since the input pulses occur at 20 μ s intervals, the time duration of the complete triple-fold code is 26.62 ms. The period between consecutive code generations is 10 seconds. The triple-folded Barker code thus generated simplifies the modulator requirements of the RF section and is readily instrumented.

F. Digital Circuitry

There are several problems, peculiar to this payload, associated with the design of the digital electronics in general and the Barker code generator in particular. Aside from the need for highly stable digital circuits for the relatively difficult environmental conditions, a wide temperature variation, the extended duration of the experiment, the time degradation of the component parameters through natural causes, and accumulated radiation damage, the circuits of the Barker code generator must be ultra stable in order to always send the exact code (matched filter receiver) in the presence of the large pulsed RF flux (noise) which, in general, tends to cause false triggering of

the bistable circuit elements. Additionally, judicious placement of critical components and/or shielding to minimize the background noise is comparatively difficult because of the low system weight.

To cope with these problems, digital circuit techniques employing some new concepts have been developed. These concepts have resulted in on-board digital circuits that appear to be extraordinarily stable with respect to false triggering, parameter variation, and radiation. Paradoxically, they consume about two orders of magnitude less power than the standard high-impedance, low-power circuits currently being utilized throughout the aerospace industry for satellite instrumentation.

The essential idea is to design the circuits for relatively large power consumption, that is, with low-circuit impedances that result in highly stable circuits with greatly relaxed requirements on component parameter stability along with a high tolerance to temperature and voltage variations. The supply voltage is then "duty cycled" in a manner similar to the way in which pulses are "clocked" in a switching circuit system. A brief description of the operation of these "pulsed power" circuits (PPC)* follows.

One realization of the basic PPC bistable circuit along with the powered and non-powered equivalent circuits is shown in Fig. 33. Fig. 34 gives some of the pertinent waveforms of the circuit.

As may be seen from the circuit diagram and the associated waveforms, the capacitor which is charged to approximately +v.

* See Ref. 1, page 7; of this report.

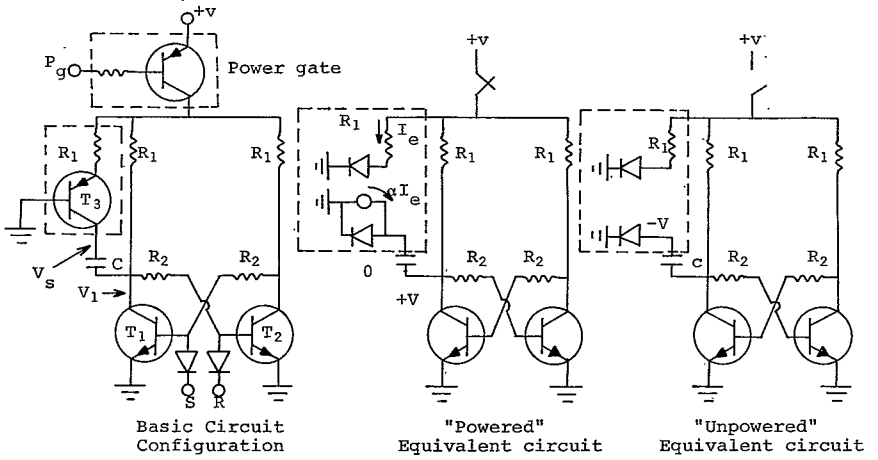


Figure 33

PULSED POWER CIRCUITS

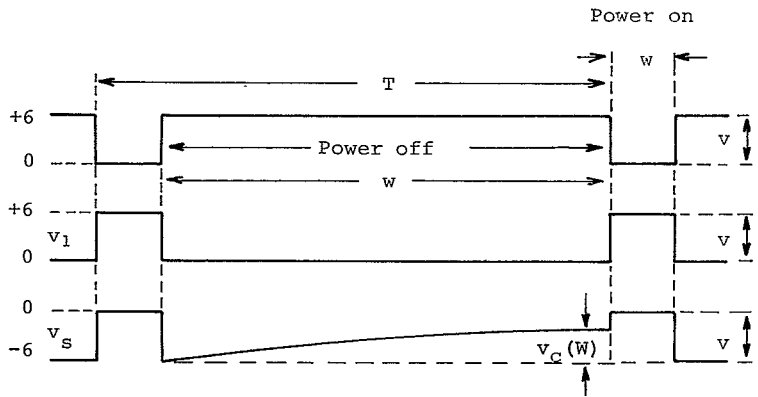


Figure 34

WAVEFORMS OF PULSE POWER CIRCUITS

when the power is on, loses energy through the resistance of a back-biased collector diode when the power is off. This lost energy is replaced at the beginning of the subsequent powered phase. Since the collector of transistor T_1 is positive driven at the beginning of the power phase by T_3 , the FF is reestablished in the "correct state." On the other hand, had the circuit been in the alternate state ($v = 0$) at the end of the powered phase, the capacitor would have been uncharged, and at the end of the preceding power interval upon application of power, the collector of T would be "clamped" into low voltage state and hence the FF is reestablished in this state.

The average power consumption may be derived by expressing the supply energy per cycle as being equal to the energy dissipated in the resistors plus twice the energy stored on the capacitor. If the FF is not changing state, then the energy dissipation per cycle is

$$E_{\text{cycle}} = v^2 \left[\frac{2}{R_1} + \frac{1}{R_1 + R_2} \right] w + 2cv^2 (1-\alpha^2) \text{ "1" state}$$

where $\alpha = \frac{v_c(w)}{v}$ [19]

or

$$E_{\text{cycle}} = v^2 \left[\frac{2}{R_1} + \frac{1}{R_1 + R_2} \right] w + 0 \text{ "0" state}$$

If the FF changes state:

$$E_{\text{cycle}} = v^2 \left[\frac{2}{R_1} + \frac{1}{R_1 + R_2} \right] w + \frac{1}{2} [2cv^2 (1-\alpha^2) + cv^2] \text{ [20]}$$

where the factor of $\frac{1}{2}$ reflects the fact that the capacitor has no charge when storing zeros.

From [20] the power level is:

$$P_L \approx \left\{ \frac{v^2}{R_1} (2w) + \frac{cv^2}{2} [2 (1-\alpha^2) + 1] \right\} \frac{1}{\tau} \quad [21]$$

or

$$P_L \approx \frac{v^2}{R_1} \left\{ 2w + \frac{R_1 C}{2} [2 (1-\alpha^2) + 1] \right\} PRF \quad [22]$$

assuming that $R_1 \gg R_2$ and the FF charges state each clock period.

An approximate numerical value for the power level of Eq. [22] may be obtained by recognizing that, in order to charge the storage capacitor, the power pulse (w) must be equal to about three time constants. That is:

$$w \approx 3R_1 C \quad [23a]$$

Substituting this value for w into [22] gives:

$$P_L = cv^2 \left\{ 6 + \frac{1}{2} [2 (1-\alpha^2) + 1] \right\} PRF \quad [23b]$$

And if it is assumed that the value of α is equal to about $1/2$, that is, if the storage capacitor voltage is left to decay to about one-half of its original value before replenishing the charge, then [23b] may be expressed as:

$$P_L = cv^2 (7.25) \times PRF \quad [23c]$$

or

$$P_L \approx 7cv^2 \times PRF \quad [23d]$$

Aside from the substantial power reduction afforded by this approach, there are several other important features. Among these are:

1. The PPC bistable element and the associated "trailing-edge logic" used exhibit noise immunity from various spacecraft "pickup" phenomena due not only to the use of "trailing-edge logic" and the reduced high-frequency gain caused by the storage capacitor, but to the fact that the circuit is not energized (and hence not subject to false trigger) a large fraction of the time. The numerical value of the increased noise immunity factor appears to be approximately equal to the inverse of the power duty cycle.

2. Wide temperature variation design. The design criteria of low power PPC bistable circuitry is greatly enhanced because the circuitry is not energized a large percentage of the time and, therefore, the circuitry may be designed to draw a relatively large amount of power during the power phase. This, in turn, allows the use of lower circuit-impedance levels, relaxation of many of the stringent component requirements of heretofore low-power circuit realizations.

3. Radiation resistance. Although the radiation damage is a complex one and many of the parameters are unclear, nevertheless certain general relationships are known¹. In particular, ionization effects and the resulting transient increases in leakage current and degradation of current gain should be less deleterious due to the fact that a major portion of the system built with these techniques is unenergized most of the time.

1. D. S. Peck, R. R. Blair, W. L. Brown, and F. M. Smits: BSTJ, vol. XLII #1 - "Surface Effects of Radiation on Transistors," Jan. 1, 1963.

G. Telemetry

There are two complete telemetry systems aboard the spacecraft. The beacon telemetry system measures information that is concerned with the initial performance of the spacecraft, while the main telemetry system transmits performance information of long-term interest. The parameters measured by both systems are tabulated in Table V.

The time to transmit a main telemetry "cycle" is 1440 seconds. This "cycle" consists of 144 bits of information divided into eight "groups" of 18 bits. This format is characterized in Fig. 35a. As shown, the first bit of each group is a "drop-out" (no transmission is made) which may be used to synchronize the incoming information. The next three bits indicate the identity of the "group" being transmitted and, therefore, the identity of the remaining 15 bits in the group. The last 14 bits contain two seven-bit telemetry "words" which are the digitalized result of a particular measurement (i.e., temperature, power, etc.).

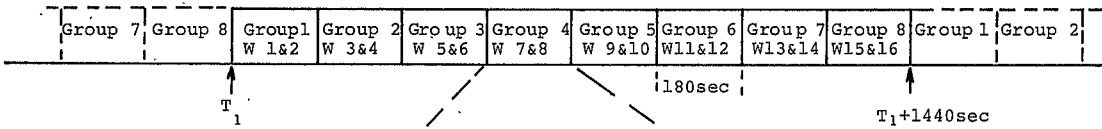
The "spikes" indicated in Fig. 35b represent Barker code transmissions of 26.62 ms duration. The positive-going spikes are interpreted as a "1" transmission, while the negative represents a "0" transmission. The "1" transmission is defined as a transmitted barker code while a "0" is an inverse Barker code.

The circuitry that performs the telemetry measurement function is indicated in Fig. 36. The system is composed of three sections.

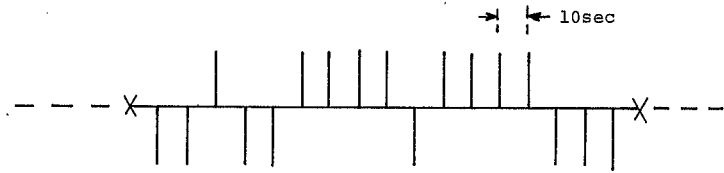
TABLE V. Telemetry Systems

BEACON TELEMETRY
(112 bits/sec)

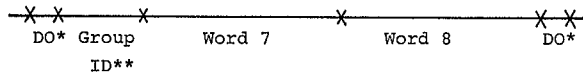
- | | |
|---------------------------------------|---------------------------------------|
| 1. Temperature (5) | 1. Temperature (5) |
| a) Solar cells | a) Solar cells |
| b) Front plate | b) Front plate |
| c) Back surface | c) Back surface |
| d) Oscillator compartment | d) Oscillator compartment |
| e) Transmitter compartment | e) Transmitter compartment |
| 2. DC Power System | 2. DC Power System |
| a) Solar cell output | a) Solar cell output |
| b) Power converter output | b) Power converter output |
| c) Energy storage
(capacitor bank) | c) Energy storage
(capacitor bank) |
| 3. 100MC Power Level | 3. 100MC Power Level |
| 4. 300MC Power Level | 4. 300MC Power Level |
| 5. Attitude (8) | 5. Attitude (4) |
| a) 4 forward hemisphere | a) 4 forward hemisphere |
| b) 4 side looking | |
| 6. Package Separation | |



a) Cycle



b) Typical group



* DO-drop out
 ** ID-identification

Figure 35 MAIN TELEMETRY FORMAT

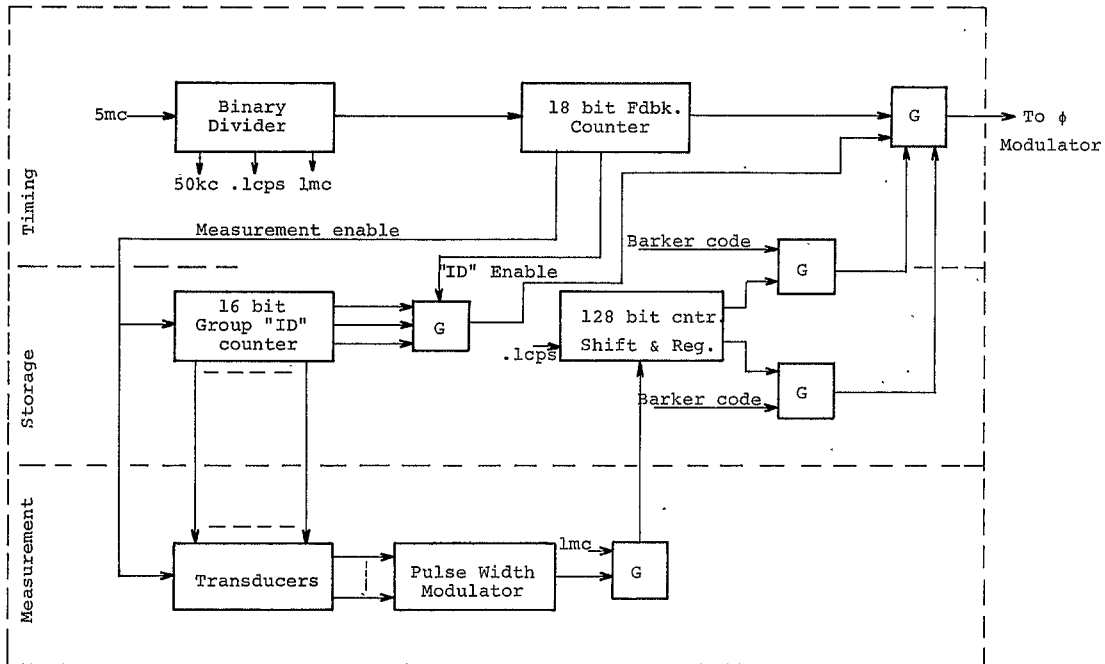


Figure 36 MAIN T/M SYSTEM

The measurement section converts the data from the transducers into digital form and serves as a multiplexer and analog-to-digital converter. The storage section stores the digital information until it is shifted-out and transmitted. The third section is a programmer that performs the necessary timing operations.

1. System properties. For initial tracking, the satellite beacon-transponder will provide a target for a ground-based radar to measure the satellite coordinates, preferably out to a million kilometers. Measurement of the satellite range and bearing at several times will allow one to compute the satellite velocity.

System calculations were based on the following assumptions:

a. For radar

power = 5×10^6 w peak

antenna gain = 46 db

antenna area = 516 m^2

b. For transponder

power = 1 w peak

antenna gain = 0 db

antenna area = 0.01 m^2

pulse rise time = $1 \mu\text{s}$

Assuming no antenna losses and a system noise temperature of 290° K , the following system parameters were obtained:

TABLE VI

R [Km]	$P_{\text{satellite}}$ [dbm]	P_{ground} [dbm]	T_R for $S/N=1$	$\delta T_R/T_R$
10^4	-28	-94	1 μ s	$\sim 10^{-5}$
10^5	-48	-114	1 μ s	$\sim 10^{-6}$
10^6	-68	-134	100 μ s	$\sim 10^{-5}$

Thus there is an optimum range of about 10^5 km where the fixed errors in the system and the noise-limited error in the receiver combine to produce a minimum relative range error of about 10^{-6} which, according to the orbital calculations, will allow a prediction of the satellite period to within a few minutes of time, assuming no other uncertainties or perturbations. In addition, a measurement of the satellite angular position within approximately 0.2° will allow prediction of the satellite anomaly, or offset, to within about 1 hour, and the inclination of the plane of the satellite orbit to within 0.04° .

2. Beacon-transponder electronics. The beacon-transponder will periodically transmit beacon pulses giving telemetry information except when the transponder is triggered by a pulse from the ground; then the transponder will transmit immediately a different sequence of pulses permitting ranging information to be obtained.

The beacon-transponder is made of three basic parts: a transmitter, a receiver, and a logic net, as shown in Fig. 37.

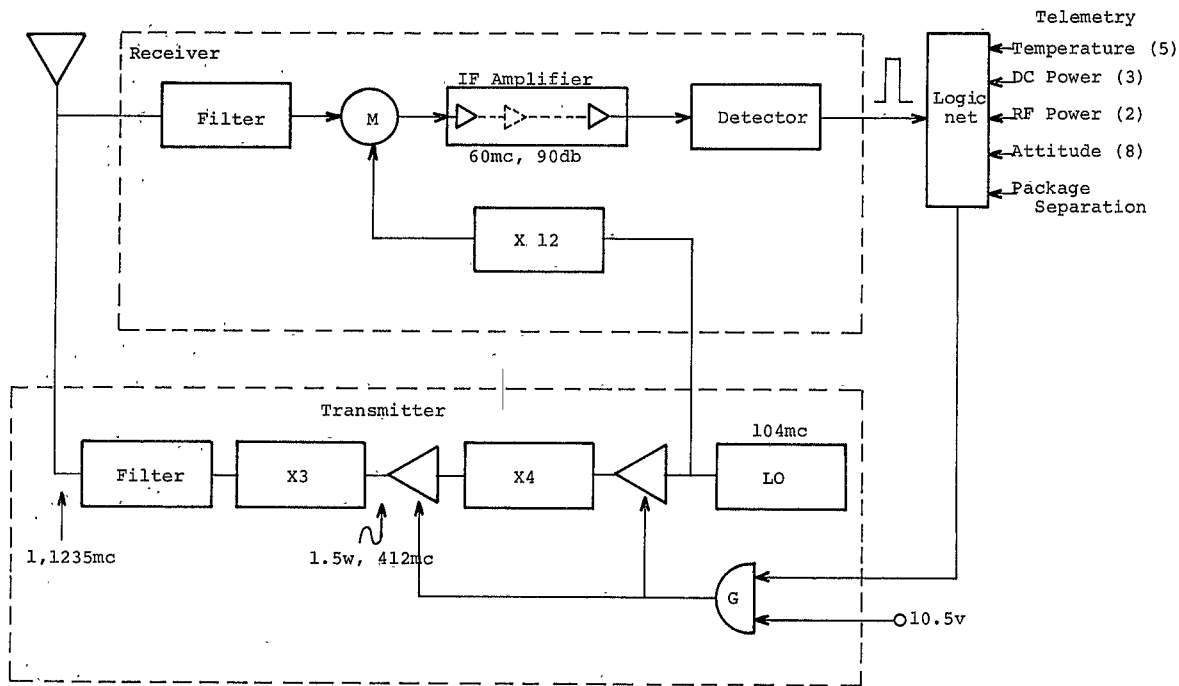


Figure 37 BEACON TRANSPONDER

The transmitter generates approximately one w of pulsed power at 1235 MC. The transmitter was a crystal-controlled oscillator and a solid state multiplier-amplifier chain, which uses high-frequency silicon transistors to generate over a watt of power at 412 MC, where the signal is tripled by a varactor to 1235 MC and passed through a filter to the antenna. The receiver consists of a crystal mixer with a 1235 MC snap-diode local oscillator, a 60 MC, 90 db, i-f amplifier, and a detector. The logic net generates pulses, both beacon-telemetry pulses whose positions are modulated by certain telemetered voltages and transponder pulses whose positions are synchronized to a received pulse. Certain basic performance specifications of the beacon-transponder are listed below:

Frequency	L-band
Power	1 w pulsed*
Duty factor	0.01
Weight {	Electronics 3 oz
	Batteries 3 oz
Lifetime (minimum)	3 days

* Can be increased with additional weight

The construction of the beacon prompted the development of a new, efficient, versatile radio-frequency circuits' packaging technique. Characteristics of the packaging technique are:

- (1) packaging of transistors on one side of a printed circuit board with other components on the reverse side;
- (2) component

point-to-point wiring with a minimum of printed wiring, eliminating excess connections; (3) packaging of stages in a long, thin, waveguide package, minimizing spurious feedback; and (4) maintenance of a common ground plane on most of one side of the printed circuit board. In addition, the beacon radio-frequency circuits are designed with no variable elements. In circuits where the tolerances are critical, it was found feasible to first use variable elements in the circuit, and then replace them with fixed elements with little loss in performance. Consequently, the beacon-transponder, incorporating 13 transistors, 4 diodes, and a crystal, easily occupies a 2 in. by 5 in. printed circuit card and weighs about 3 oz.

H. Beacon Telemetry

The parameters telemetered by the beacon electronics are given in Table V. These measurements contain the performance indices that are indicative of spacecraft operation from launch to approximately three days (1 million nm).

1. Format. The telemetry format as indicated in Fig. 38 is basically a "pulse-position-modulation" (PPM) system. The time interval between successive one ms pulses varies between one and 10 ms and is a function of the telemetered information. The first pulse in the sequence, which is 5 ms long, serves as a beacon pulse and enables the vehicle to be tracked. This beacon format repeats at one-second intervals except when the system is in the transpond mode. In this case, the PPM format is an eight-pulse square wave burst with a characteristic frequency of 500 cycles/sec.

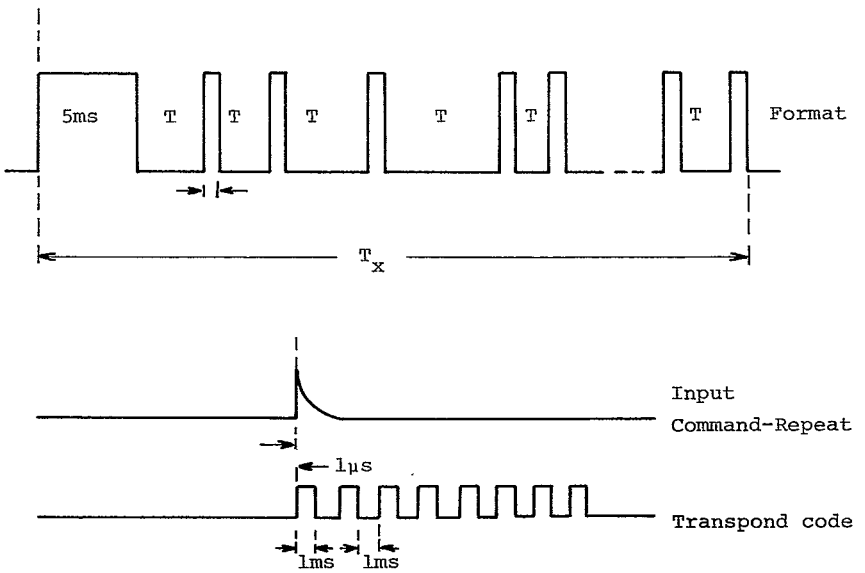


Figure 38 BEACON T/M FORMAT

The PPM format was chosen since its inherent accuracy suffices (about 1 pct) and is relatively easy to instrument. Further, this modulation system has a fixed-transmitter duty cycle which is independent of the number of bits transmitted and, therefore, easier to design for a given battery-powered operating life.

2. System description. The block diagram of the beacon electronics is shown in Fig. 39. The system consists of a timing section that supplies the one cps-5 ms marker pulse, and a measurement and encoding section which converts the transducer information into the pulse-position modulation format.

Briefly, the system operates as follows. At the end of the marker pulse a counter is indexed and drives the transducer multiplexing circuits which in turn drive a pulse-width modulator consisting of two one-shot multivibrators. Each time the multivibrators "fire," the counter is indexed until it cycles through all 16 positions at which time the system "shuts down" until either the next marker pulse or another transponder pulse is received from earth.

The system is designed such that the transponder mode dominates; i.e., when a transpond pulse is received from the ground, the beacon mode is automatically interrupted.

II. Receiver and Detector

A. System Description

When the spacecraft is in the vicinity of superior conjunction, a receiver is needed that will enhance the s/n ratio of

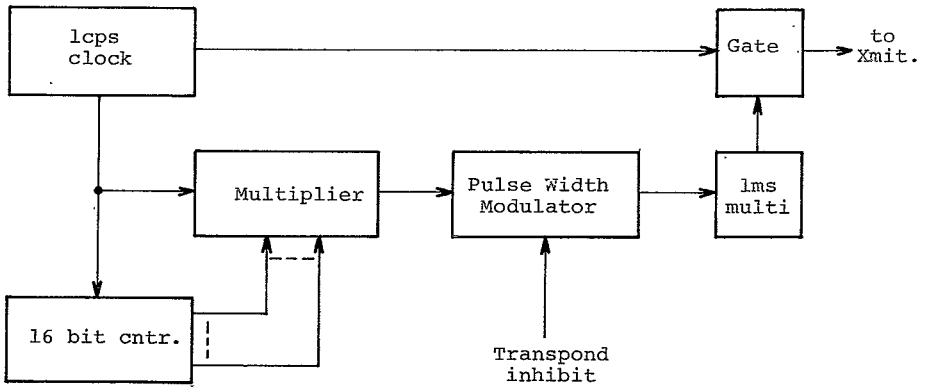


Figure 39 BEACON T/M SYSTEM

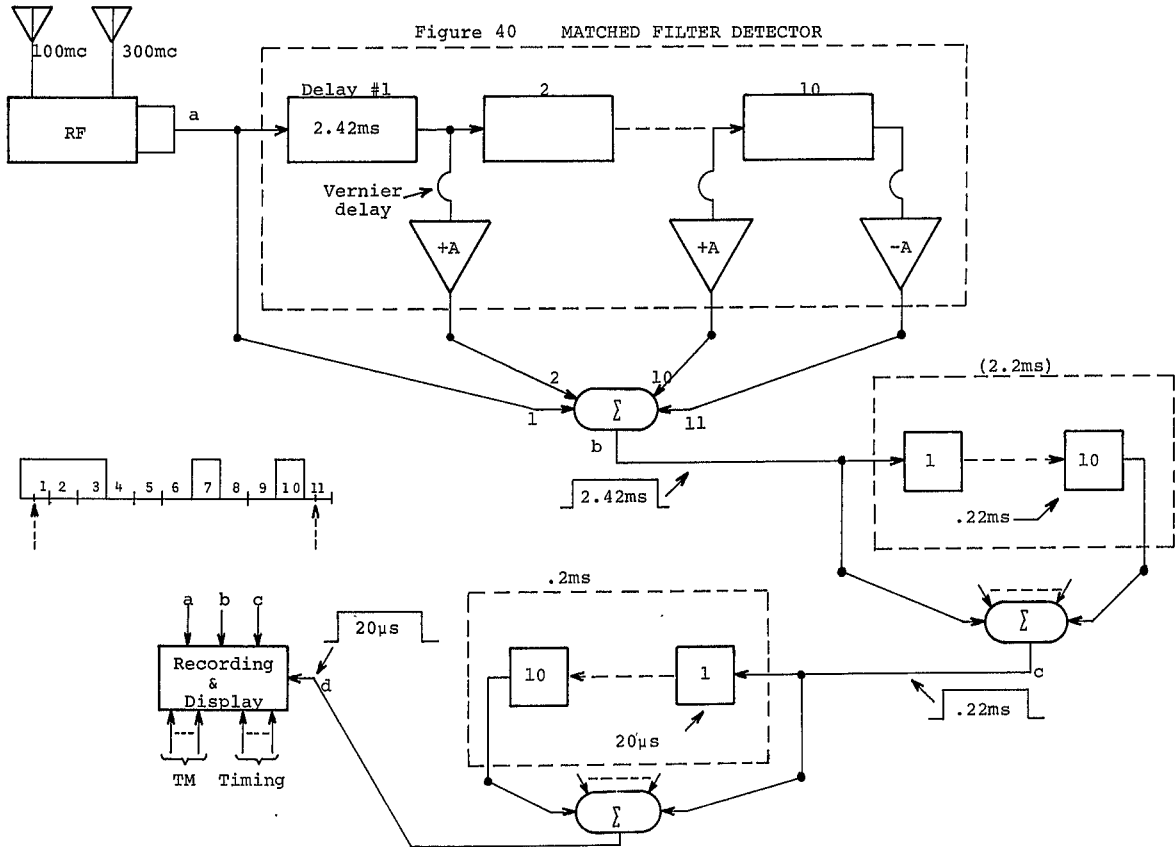
the incoming signal. A realizable "matched filter" utilizing quartz delay lines is a means of providing this enhancement.

The receiver's primary function is to measure the differential time delay between the two simultaneous spacecraft transmissions. To facilitate this measurement, the receiver must compensate for the Doppler shift, compress the signal into a pulse form that is more readily detectable, and record the signals so that telemetry information can be extracted by post-data reduction.

When the transfer function of a filter exactly equals the complex conjugate of the expected signal, it is said to be "matched" to the signal. Thus, by having a priori knowledge of the received signal, a filter can be designed that will reject all signals except that class which satisfies the predetermined criteria.

In coding the spacecraft signal, as explained in sections I., E, F, G, H, the signal energy has been spread over a 26.62 ms duration. By matching the code in the receiver, the signal energy is compressed into a pulse that is 1331 times narrower (20 μ s pulse). This not only improves the time resolution of the received signals but also enhances the signal-to-noise ratio by about 30 db.

A block diagram of the "matched filter" receiver that has been designed for the reception of the spacecraft signals is shown in Fig. 40. The system is composed of three sections. The RF section amplifies the signal from the antenna, mixes this signal down to an IF, and removes the Doppler content. The second section contains the tapped-quartz delay lines which "unfold" the code, thereby compressing it into a central high-amplitude pulse. The



last section measures the time delay between marker pulses and records them for later analysis.

B. Matched Filter Detector

The IF input to the delay lines shown in Fig. 40 as signal "a" is converted by the input transducer into acoustical energy. This propagates down the line at approximately 5900 meters/sec. By placing taps along the line, the input signal can be "picked-off," electrically identical to that inserted but delayed in time. The tap outputs are then electronically joined through a weighting network, resulting in a compression of the input pulse.

This compression is performed three times, corresponding to each of the three folds associated with the Barker code. The actual matching of the input signal is performed by the electronics associated with each tap. Thus, if the first bit of the third fold was a "1" (corresponding to 0° phase shift), then the tap electronics adds the signal into the weighting network with no further phase shift. However, where a "0" (corresponding to a 180° phase shift) is expected, the tap adds 180° of phase shift in order to bring the "1's" and "0's" into phase alignment. Therefore, when the correct signal is present, all the inputs to the weighting network are in phase, and the output, being a linear superposition of the inputs, will be a maximum.

The input signal consisting of 1331 phase reversals (bits) is inserted into the 24.2 ms delay line (tapped at 2.42 ms intervals), and when the signal is exactly aligned the weighting network outputs increase significantly. This increase contains 121

phase reversals corresponding to the second fold of the code and is inserted into the 2.2 ms delay line which is tapped at 200 μ s intervals. When the signal in this line is aligned, the weighting network produces an output signal that is 200 μ s long. This signal, which corresponds to the first fold of the Barker code, is inserted into the 200 ms delay line which is tapped at 20 μ s intervals. The output from this line is a 20 μ s signal that has virtually all of the energy of the original 26.62 ms signal compressed within it. This pulse corresponds to the least significant bit of the impressed code and is the governing condition that determines the ultimate resolution of the differential measurement to be within 20 μ s.

Since the spacecraft transmits energy at two different frequencies, compression must be performed twice; once for each arriving frequency. Ordinarily this would entail using two sets of "matched filters;" however, by choosing high-bandwidth quartz delay lines, the signals may be multiplexed into the one set of lines. The 100 mcps signal is put on the line at 32 mcps and the 300 mcps signal is inserted at 28 mcps.

The compressed pulses are recorded on tape and the time differential is measured by starting a precision clock upon the arrival of the 30 MC transmission and stopping the clock after the 100 MC pulse has arrived. This time is also stored on tape and printed-out in real time in order to get "quick-look" data. The telemetry information, as indicated in section I.G., is contained in the final pulse compression and is either a "1" or a "0".

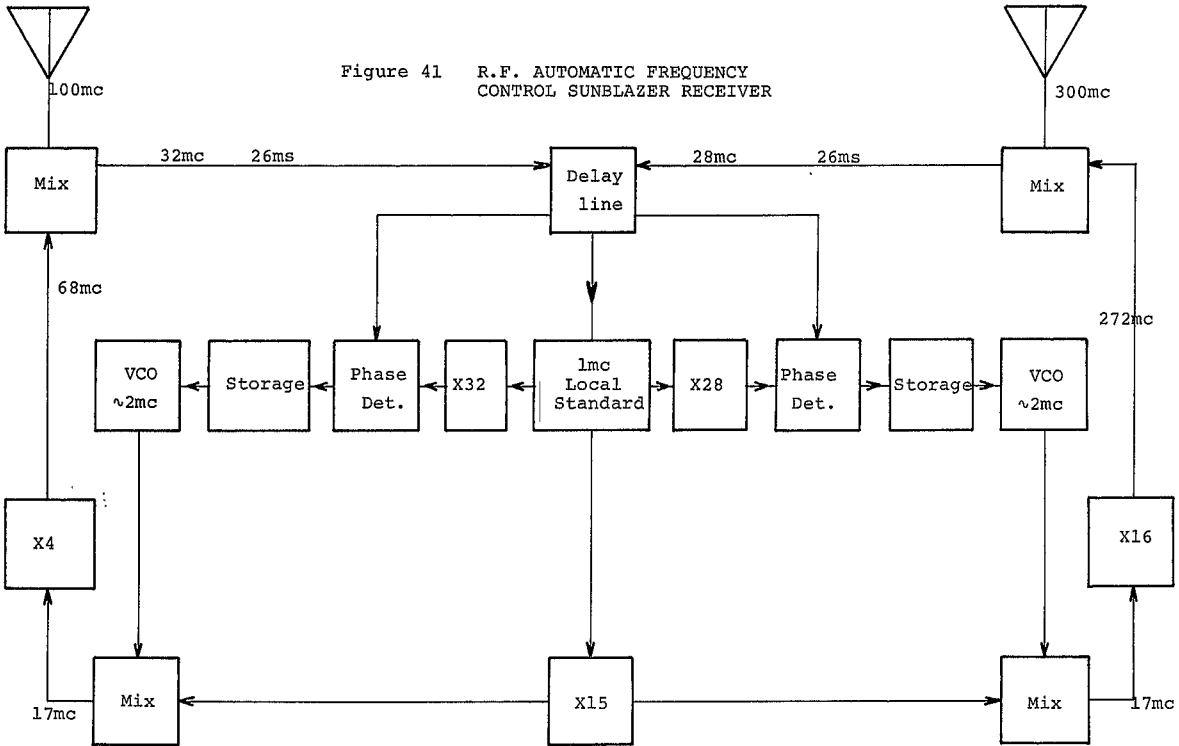
C. Receiver - RF System

The type of receiver and the complexity of its design are generally determined by the system signal-to-noise ratio at the time of detection. In regions of high s/n a phase detector in one of its many configurations will perform signal video detection.

For the case of a low signal-to-noise ratio, both signal detection and pulse compression require the use of matched filters. The detector may be realized by a tapped quartz delay line of appropriate design. Typically, quartz delay-line performance is optimum at approximately 30 MC. A phase-locked frequency-translating system shown in Fig. 41 translates the RF carrier to the 30 MC frequency range.

The phase-locked system removes frequency variations due to spacecraft local oscillator drift and Doppler frequency changes. The carrier delay-line output pulse is compared against a local standard in a phase detector. The phase detector output is processed in a predictor/storage network, whose output controls a precision voltage-controlled oscillator (VCO). The frequency of the VCO is controlled in a manner that removes average carrier frequency variations. The quartz delay line operates on two frequencies and, in general, each frequency should have its own phase-locked loop. However, if it is assumed that the received frequencies are exact multiples, then only one phase-locked loop is required to control both sections of the receiver front end.

Figure 41 R.F. AUTOMATIC FREQUENCY CONTROL SUNBLAZER RECEIVER



APPENDIX A

Thermal Transfer and Radiation from a Thin Circular
Plate Source--Thin Cylindrical Shell Radiator

I. Introduction

For the Sunblazer satellite, it is of interest to calculate the radiative properties of thin shells. In the configuration of Fig. 42, which is a simplified drawing of the Sunblazer satellite, there are two such shells. The first is the front plate, a thin plate which is covered with solar cells. The second is the cylinder, a thin shell which radiates excess heat into space.

II Summary

Assuming no radiative heat transfer within the cylinder, the temperature on the shells and the rate of radiation of the shells is determined solely by a dimensionless variable ζ , where:

$$\zeta = 1/2 \frac{\epsilon\sigma}{Kt} T_0^3 x^2$$

ϵ = Emissivity of shell (0.85 for aluminum)

σ = $5.67 \cdot 10^{-12}$ watts/cm²-°K⁴

K - Conductivity of shell (2.05W/cm-°K for aluminum)

t - Thickness of shell

T₀ = Temperature of shell at free end

x = Distance along shell (length on cylinder

or radius on plate)

[1]

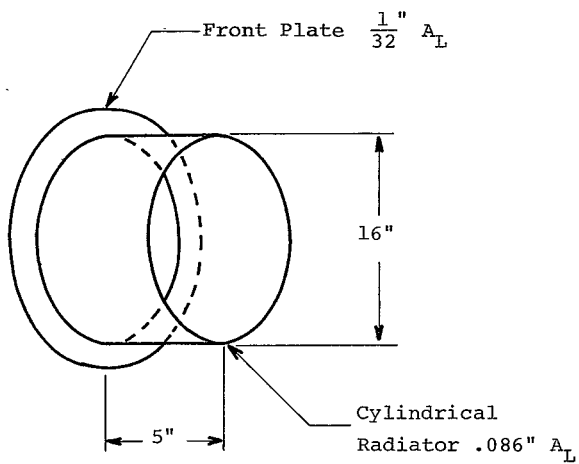


Figure 42

THE RADIATOR GEOMETRY

The smaller ζ is, the closer the system approximates an isothermal system. In terms of ζ , the temperature on the cylinder is given by:

$$T = T_0 \left(1 + \zeta + \frac{2}{3}\zeta^2 + \frac{26}{45}\zeta^3 + \frac{116}{315}\zeta^4 + \frac{251}{1050}\zeta^5 + \dots \right). \quad [2]$$

The heat conducted down the cylinder is given by:

$$H = K2\pi r t \frac{dT}{dZ} = K \frac{4\pi r t T_0}{Z} \left(\zeta + \frac{4}{3}\zeta^2 + \frac{78}{45}\zeta^3 + \frac{464}{315}\zeta^4 + \dots \right) \quad [3]$$

$$H = 2\pi r Z \epsilon \sigma T_0^4 \left(1 + \frac{4}{3}\zeta + \frac{78}{45}\zeta^2 + \frac{464}{315}\zeta^3 + \frac{251}{210}\zeta^4 + \dots \right), \quad [4]$$

where r = radius of cylinder.

The temperature on the plate is given by:*

$$T = T_0 \left(1 + \rho + \frac{1}{2}\rho^2 \zeta + \frac{1}{3}\rho^2 \zeta^2 + \frac{5}{48}\rho^2 \zeta^2 + \frac{1}{72}\rho^2 \zeta^3 + \dots \right) \quad [5]$$

$$T = T_0 + T_0 \cdot \rho \Sigma_1, \quad [6]$$

where

$$\rho = \frac{1}{4} \left[\frac{\epsilon \sigma}{K t} T_0^3 r^2 - \frac{\alpha Q}{K t T_0} r^2 \right]. \quad [7]$$

α = Absorptivity of front plate

Q = Heat flux per unit area incident on front plate

$$\Sigma_1 = 1 + \frac{1}{2}\zeta + \frac{1}{3}\zeta^2 + \frac{1}{72}\zeta^3 + \dots \quad [8]$$

The heat conducted out of the plate is given by:

$$H = K2\pi r t \frac{dT}{dr} = 4\pi K t T_0 \rho \Sigma_2, \quad [9]$$

where

$$\Sigma_2 = 1 + \zeta + \frac{1}{3}\zeta^2 + \frac{1}{18}\zeta^3 + \dots \quad [10]$$

* NOTE: For this calculation we have assumed a plate 16" in diameter, ending at the beginning of the cylinder. A slightly larger plate will have a similar temperature profile, depending similarly upon ζ .

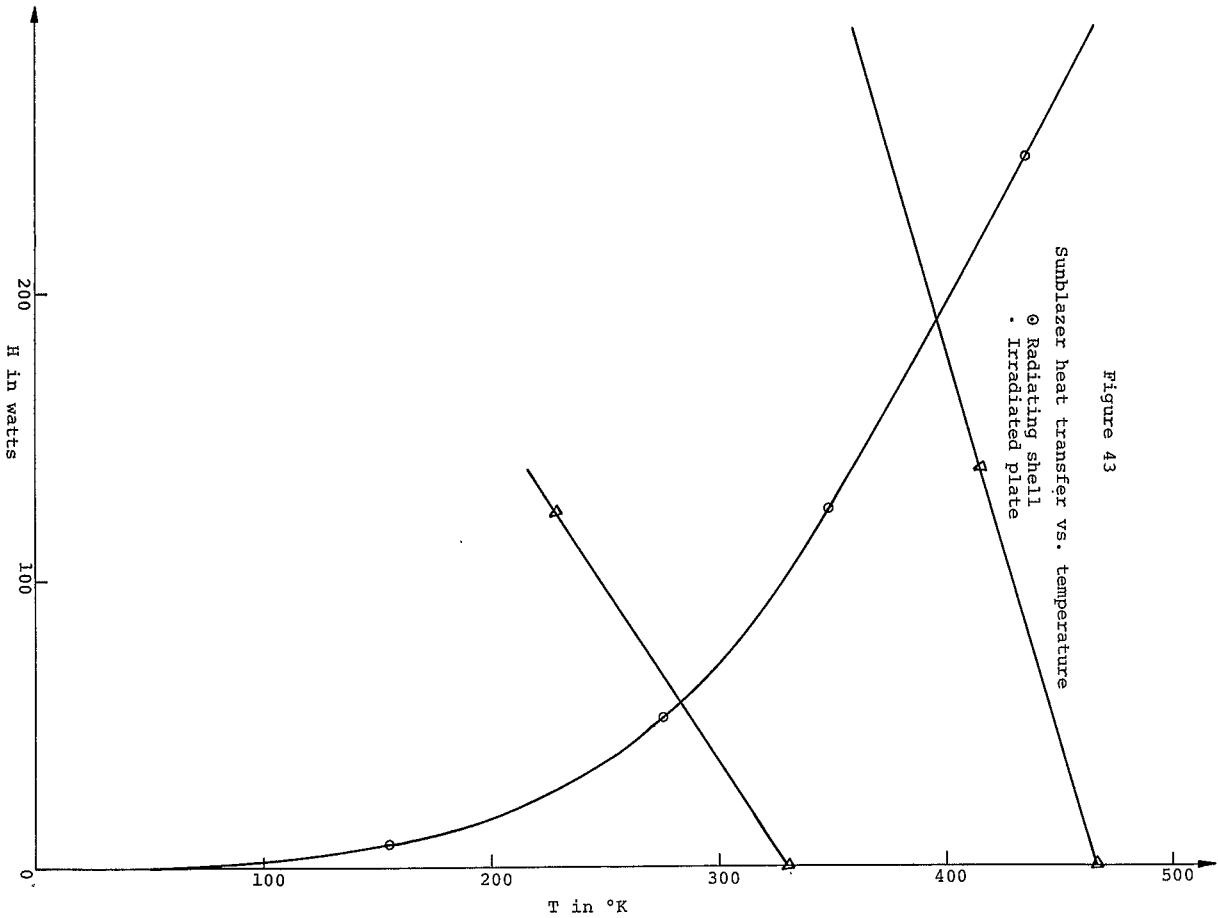


Figure 43

Defining

$$T_{\infty} = \frac{1}{4} \sqrt{\frac{\alpha Q}{\epsilon \sigma}} \quad [11]$$

equations [6], [7], [10] and [11] can be solved to give

$$H = 8\pi Kt \frac{\Sigma_2 \zeta}{1+2\Sigma_1 \zeta} (T_{\infty} - T) \quad [12]$$

and

$$\Delta T = \frac{2\Sigma_1 \zeta}{1+2\Sigma_1 \zeta} (T_{\infty} - T). \quad [13]$$

By plotting H vs. T from equations [2], [3] and [12], the common operating point of the cylinder and the plate can be found, as shown in Fig. 43.

Then the temperature rise along the cylinder and the plate can be found from equations [2] and [13]. The temperatures on the cylinder and plate have nearly parabolic dependence on distance, as shown in Fig. 44.

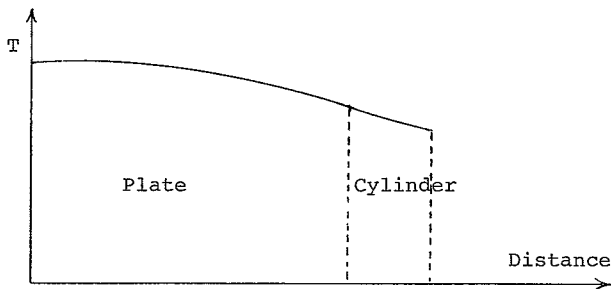


Figure 44. Temperature profiles on cylinder and plate

If the cylinder were at a constant temperature T, it would radiate heat at a certain rate R. The actual rate of radiation divided by R gives an efficiency

$$\eta_1 = \frac{1 + \frac{4}{3}\zeta + \frac{78}{45}\zeta^2 + \frac{464}{315}\zeta^3 + \frac{251}{210}\zeta^4 + \dots}{(T/T_{\infty})^4} \quad [14]$$

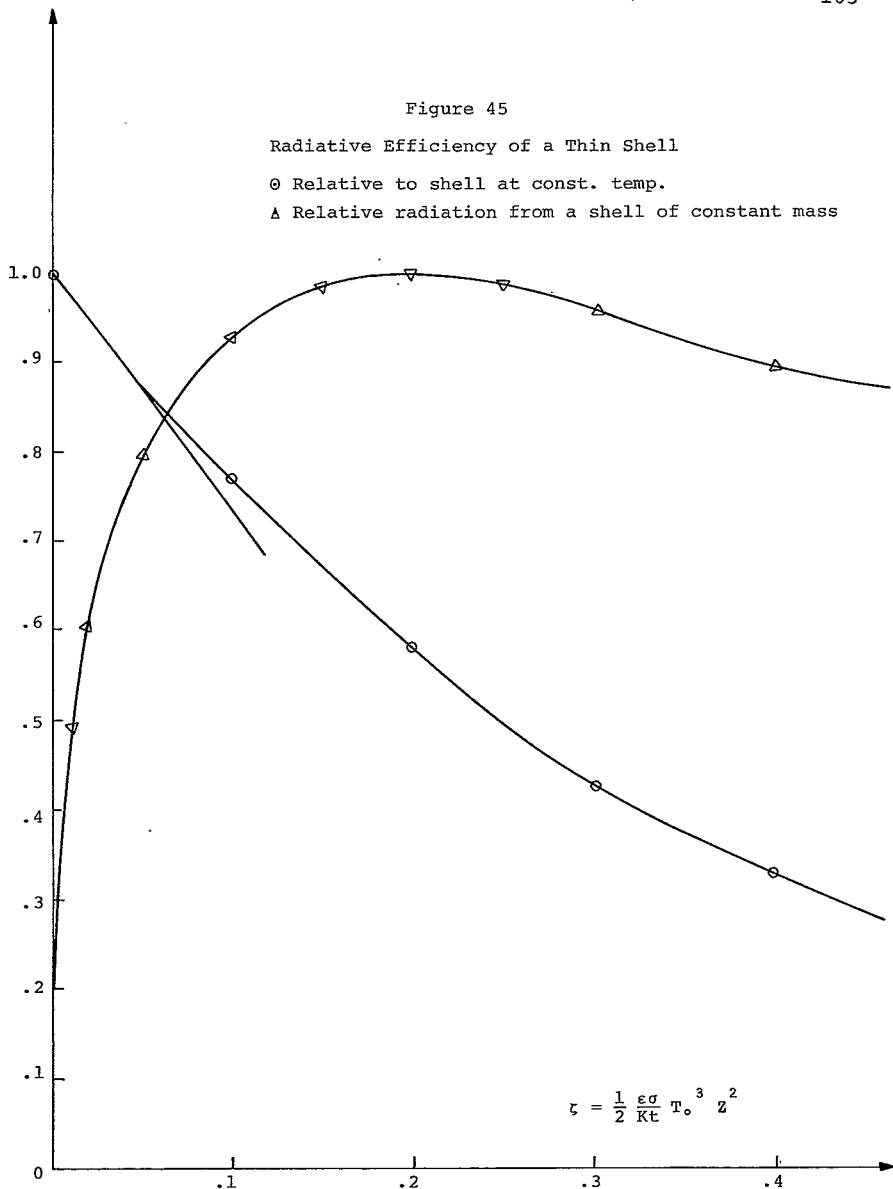
which is shown in Fig. 45.

Figure 45

Radiative Efficiency of a Thin Shell

○ Relative to shell at const. temp.

△ Relative radiation from a shell of constant mass



If we have cylinders of given mass and wish to maximize the heat radiated from the cylinder by optimizing the x to t ratio, we get the following equation,

$$\eta_2 = \frac{\zeta^{1/3} \left(1 + \frac{4}{3}\zeta + \frac{78}{45}\zeta^2 + \frac{464}{315}\zeta^3 + \frac{251}{210}\zeta^4 + \dots\right)}{0.422(T/T_0)^3} \quad [15]$$

Thus a cylinder of any mass will radiate a maximum amount of heat for $\zeta=0.20$.

III Derivation of Equations

We have assumed no radiative heat transfer within the cylinder. This is a fairly good assumption because [1] in the inside of the cylinder contains electronic packages which obstruct heat flow, [2] the radiative heat transfer within the cylinder will be less than the conductive heat transfer and [3] given the above solution, we can easily obtain a good approximation to the complete solution by (a) assuming the given temperature distribution, (b) calculating the radiative heat inputs to the various areas of the shell, and then (c) re-calculating the temperature distribution (keeping (b) constant). This process could be iterated to obtain a closer approximation.

For the cylinder with no radiative heat transfer, the equation of heat balance is

$$\frac{d^2T}{dX^2} = \frac{\epsilon\sigma}{Kt} T^4 \quad [16]$$

Assuming a solution of the form

$$T = T_0 (1 + aX^2 + bX^4 + cX^6 + \dots) \quad [17]$$

Expanding [16] and equating like powers of X leads directly to equation [2]. Differentiating [17], we get

$$\frac{dT}{dX} = \frac{2T_0}{X} (aX^2 + 2bX^4 + 3cX^6 + \dots) \quad [18]$$

which is equivalent to [3].

For the front plate with heat input, from the sun, the equation of heat balance is

$$Kt \frac{d}{dr} \left(r \frac{dT}{dr} \right) - \epsilon \sigma r T^4 + \alpha Qr = 0 \quad [19]$$

By similar methods, we obtain Equations [5] through [13]. Because the front plate tends to equilibrium at a temperature near the maximum possible temperature, one of the properties of the solution is that the rate of heat conduction out of the plate is nearly a linear function of temperature drop.

DOCUMENT REQUEST

NASA SCIENTIFIC AND TECHNICAL INFORMATION FACILITY

OPERATED BY INFORMATICS TISCO, INC

POST OFFICE BOX 33 COLLEGE PARK, MARYLAND 20740 TELEPHONE (301) 778-2121

DOCUMENT REQUESTED

A NASA ACCESSION NUMBER	B. NACA/NASA REPORT NUMBER
1 N65 32722	OR
C (PLEASE DO NOT WRITE IN THIS SPACE)	
D. COPY TYPE REQUESTED	
16 case file	<input type="checkbox"/> MICROFICHE <input checked="" type="checkbox"/> FULL SIZE

REQUESTER IDENTIFICATION

E REQUESTER'S FACILITY IDENT NO	F REQUESTER'S CONTRACT NO
2523	
G AUTHORIZED SIGNATURE AND DATE	
Ellen Davis Dec 8, 1975	

OTHER BIBLIOGRAPHIC INFORMATION (ESSENTIAL IF ITEMS "A" AND "B" ARE UNKNOWN)

H DOCUMENT TITLE	
I DATE OF REPORT:	J. AUTHOR(S)
K CORPORATE SOURCE:	L CORPORATE REPORT NO.
	M CONTRACT NO:

N. MAILING LABEL (must be imprinted on all copies, include zip code)

Ellen Davis

NTIS

NOTE: For prompt service, please follow instructions on back of last copy.

1. SHIPPING COPY

RESPONSE TO DOCUMENT REQUEST

(See item checked below for the specific reply to your request)

THE DOCUMENT YOU REQUESTED:

MAY BE OBTAINED FROM:

- (1) Superintendent of Documents, U.S.G.P.O., Washington, D.C. 20401.
 (2) National Technical Information Service, Springfield, Va. 22150
 (3) Defense Documentation Center, Cameron Station, Alexandria, Va 22314
 (4) _____

IS OUT OF STOCK AND NOT REPRODUCIBLE BECAUSE

- (5) Copyrighted (8) Not suitable for reproduction.
 (6) Journal Article (9) Source prohibits reproduction.
 (7) Purchase Item, contact source

HAS DISTRIBUTION LIMITATIONS WHICH PREVENT US FROM SATISFYING YOUR REQUEST

Available from the Facility to:

- (10) NASA only (12) U.S. Government Agencies only
 (11) NASA and its contractors (13) U.S. Government Agencies and
only Contractors only
 (14) Classified, our records do not indicate adequate clearance, contact your cognizant contracting agency.
 (15) Classified document in Category _____; our records do not indicate that your organization has been certified access to that category.
 (16) Non-NASA document and therefore available from the Facility only to NASA and its contractors, our records do not indicate that you are registered with us as a NASA contractor
 (17) Source controls and monitors all distribution

IS NOT AVAILABLE FOR THE FOLLOWING ADMINISTRATIVE REASON:

- (18) Not available outside U.S.
 (19) Requires approval of another Government agency for release (Serv. Rept.), this approval is being sought; you will be notified
 (20) Approval sought in #19 has been denied
 (21) Contains proprietary information, requiring approval of responsible NASA Office for release (Spec. Rel.), this approval is being sought; you will be notified
 (22) Approval sought in #21 has been denied
 (23) Obsolete, withdrawn from circulation
 (24) Out of subject scope, not retained in Facility's collection
 (25) Out of print, not to be reprinted or reproduced
 (26) Repeated attempts to obtain have been unsuccessful

IS NOT YET AVAILABLE

Request again when announced in *STAR* or *CSTAR* journals

- (27) Availability is under review (29) Not yet published
 (28) Review Copy or Advance Copy stage of publication
 (30) Out of stock, being reprinted, will be forwarded
 (31) Not in Facility's collection, action has been taken to obtain copies, you will be notified

IS INADEQUATELY IDENTIFIED

- (32) Please furnish correct NACA/NASA accession number or report number, or additional bibliographic information
 (33) Accession number or report number cited is not valid; check reference.

IS NOT AVAILABLE IN COPY TYPE REQUESTED

- (34) Available in microfiche only a microfiche is enclosed
 (35) Available in printed copy only.

IS NOT AVAILABLE IN MULTIPLE COPIES

- (36) Enclosed is one photocopy and one microfiche; the microfiche may be utilized as a reproducible master